NEAR-SURFACE CHARACTERIZATION USING P- AND S-WAVE TOMOGRAPHY

By

MD IFTEKHAR ALAM

Bachelor (Honors) & Master of Science in Petroleum Geology & Geophysics

University of Dhaka

Dhaka, Bangladesh

2005

Master of Science in Geology.
Auburn University
Auburn, AL, USA
2011

Submitted to the Faculty of the Arts and Science
Graduate College of the Arts and Science
Oklahoma State University
in partial fulfillment of
the requirements for
the Degree of Geology
DOCTOR OF PHILOSOPHY
December, 2016

NEAR-SURFACE CHARACTERIZATION USING P- AND S-WAVE TOMOGRAPHY

Dissertation Approved:

Priyank Jaiswal, Ph.D., Chair

Dissertation Adviser

Estella E Atekwana, Ph.D.

Todd Halihan, Ph.D.

Yanqiu Wang, Ph.D.

ACKNOWLEDGEMENTS

I thank all those who, directly and indirectly, assisted me in achieving my PhD goals. I really enjoyed working with my advisor, Dr. Jaiswal. I appreciate all his support and help that he provided to me for the last five years. I would like to thank him for being patient and providing directions in forming and maturing the research ideas. Under his supervision, I have surely matured as a student and as a researcher.

My heartiest thankfulness to Dr. Estella Atekwana, Dr. Todd Halihan and Dr. Yanqiu Wang for their contributions to this research as the committee members. My knowledge of writing and presenting has been significantly improved due to Dr. Atekwana's consistent efforts. Dr. Halihan helped me in understanding the geophysical behavior of near surface materials. Finally Dr. Wang's classes helped me with the math behind the geophysics.

I want to thank the entire seismology group for helping me in conducting the seismic survey especially Salman Abbasi, Khemraj Shukla, Pouyan Ebrahimi, Brandy Michael, Brooke Briand, Afshin Aghayan and Sundeep Sharma. I am also thankful to Andrew Katumwehe, PhD and Joshua York for helping me with some of the surveys. The Boone Pickens School of Geology, Oil India, and Society of Exploration Geophysicists provided financial assistance without which this research would not have been possible.

I am also grateful to Tim Sickbert, Sandy Earls, Tabitha Schneider, Macaley Hall, and Isabella Martinez for their help, starting from equipment check-out to paperwork since the first

day I arrived at Oklahoma State University. I have been tremendously blessed to have such a great environment, all the current and former students who I have come across.

Finally, I would like to thank my parents. Without their support nothing would have been possible for me, and my siblings for all their encouragement.

Name: MD IFTEKHAR ALAM

Date of Degree: December, 2016

Title of Study: NEAR-SURFACE CHARACTERIZATION USING TRAVELTIME AND WAVEFORM INVERSION

Major Field: GEOLOGY

Abstract: Near-surface seismic application, and those that mainly investigate the first 5 m of the subsurface, have to rely on analysis of transmission coda because reflections are typically lacking. Currently, full-waveform inversion, a method of iteratively refining an initial guesses of the subsurface (the starting model) so that the field data can be replicated wiggle-by-wiggle, is considered state-of-the-art in seismic modeling. However, waveform result with acoustic (or even elastic) approximation can be highly biased in the near-surface because the transmission wavefield is distorted by high porosity and patchy fluid saturation, factors that are difficult to incorporate in the forward modeling code. A less advanced method, which only attempts to replicate the first-arrival times, known as traveltime inversion, is available but not often used as a terminal analysis methods. Traveltime inversion is less susceptible to biases from porosity and saturations but has lower resolution than full-waveform methods.

This research shows that if, in addition to the typical vertical component data, tangential component data are also acquired, the first arrival times from both components together have comparable resolution to the single-component full-waveforms. This idea is demonstrated here using a 23m long profile across two well-documented utility pipes and a poorly documented backfilled void. Tangential data are acquired with horizontal phones oriented perpendicular to the profile to capture the SH propagation mode. Compressional and shear wave velocity models (V_P and V_S respectively) from both inversion techniques is developed. The traveltime inversion refines a simplistic 1D starting model and the full-waveform inversion refines the traveltime solution. As expected, individual traveltime images from either component are incapable of resolving the targets, but the full-waveform images are. However, when V_P and V_S traveltime images are combined as a Poisson's Ratio image, targets resolution is comparable to the full-waveform inversion results.

Results for this thesis allow a practitioner to optimize resources for near-surface seismic survey. Multi-component acquisition is more difficult and expensive than a single-component survey; but multi-component traveltime processing is easier to implement than the single-component full-waveform inversion. The results may appear to question the utility of full-waveform in near surface characterization, however, full-waveforms also yield the attenuation solution, which cannot be obtained from the arrival times and is very helpful in near-surface characterization. Although the results are presented using an ultra-shallow example, they are applicable to a wider range of settings such as shear and rupture zones or even in medical imaging where all physical factors that distort waveforms cannot be incorporated in modeling.

PUBLICATION DISSERTATION OPTION

This dissertation has been divided into two sections. The first section gives a brief outline of the dissertation and introduces the scientific question that I investigated. This section also presents one manuscript that has been published and two in review for publication.

Paper I, "Alam, M.I., and Jaiswal, P., *in press*, Near Surface Characterization Using V_P/V_S and Poisson's Ratio from Seismic Refractions: Journal of Environmental & Engineering Geophysics."

Paper II, "Alam, M.I., Jaiswal, P., and Shukla, K., 2016, *in review*, Velocity imaging with Full Waveform Inversion in the ultra-shallow subsurface, results from P-wave acquisition – Part 1: Geophysical Journal International."

Paper III, "Alam, M.I., Jaiswal, P., and Aghayan, A., 2016, *in review*, Velocity imaging with Full Waveform Inversion in the ultra-shallow subsurface, results from SH-wave acquisition – Part 2: Geophysical Journal International."

TABLE OF CONTENTS

Chapter Page

LIST OF FIGURES

Figure Page

PAPER I

PAPER II

PAPER III

SECTION I

GENERAL OVERVIEW

1.1 PROJECT MOTIVATION

Remote estimation of the strength and the petrophysical (porosity – permeability) properties of the near surface (<5 m) is rapidly gaining interest in environmental, engineering and archeological applications. In laboratory settings Santamarina et al. (2005) have shown that subtle changes in soil properties, such as porosity, particle dimension, pore-fluid type and saturation, etc., can significantly alter their elastic response, implying that the seismic velocities can be a valuable remote sensing tool for near-surface characterization. The near-surface community has long relied on refractions (the early part of the transmission coda in surface seismic) for obtaining information on low-velocity weathered layer and so on. Typically the changes in slope of the first arrival times from reciprocal records are used for mapping the bedrock thickness and velocity assuming a layered-earth.

The biggest challenge in the near surface, and especially within the first 5 meters which is the focus of this study, is the lack of coherent stratigraphy. As a result, a clear slope change in first arrival trajectory is not observed, rendering the traditional refraction analysis method useless. Further, a lack of layered stratigraphy also creates a lack of reflections. Therefore, common velocity estimation based methods such as stacking velocity analysis are inappropriate. A simple

circumvention around the lack of reflections is only analyzing the transmission coda using gridded tomographic methods where the model development, in principle, is not dependent on layer-cake assumption.

Currently, full-waveform inversion, a method of iteratively refining an initial guesses of the subsurface (the starting model) so that the field data can be replicated wiggle-by-wiggle, is considered state-of-art in transmission tomography. However, waveform result with acoustic (or even elastic) approximation can be highly biased within the first few meters (hereafter referred to as ultrashallow) because the transmission wavefield is distorted by high porosity and patchy fluid saturation, factors that are difficult to incorporate in the forward modeling code. A less advanced traveltime tomography method, which only attempts to replicate the first-arrival times, is available but not often used as a terminal analysis methods. Traveltimes are less susceptible to biases from porosity and saturations but have lower resolution than the full-waveforms.

This thesis compares and contrasts the two gridded tomographic approaches – traveltime and full-waveform inversion – in an ultra-shallow setting. I show that even traveltime inversion can provide comparable resolution; however, instead of modeling only the typically acquired vertical component data, tangential data also needs to be acquired. By tangential data I imply data acquired with horizontal phones oriented perpendicular to the ray direction. I also show the pros and cons of both methods in terms of difficulty in implementation, resolution achieved and solution bias due to sensitivity to random noise. The results from my thesis will help a near-surface practitioner in optimizing resources for a near-surface survey.

1.2 PRESENT STATE OF KNOWLEDGE

In field settings, refraction studies are generally conducted with vertical-component datasets for creating P-wave velocity (V_P) models. Traditionally, refraction studies have been used for detection of the base of the weathered layer (Docherty, 1992; Lanz *et al.*, 1998) and addressing similar problems, but a limited number of studies have also shown that refractions can also be used to infer porosity and stiffness of the soil (Francese *et al.*, 2005; McBride *et al.*, 2010; Zelt *et al.*, 2006; Al-Shuhail and Adetunji, 2016). Refraction resolution is typically defined by the order of the radius of the first Fresnel Zone (Williamson, 1991; Zhang and Toksöz, 1998). Therefore, for smaller targets, the refraction models have to be refined using other, more advanced methods such as jointly with resistivity (Gallardo and Meju, 2003, 2004) and full-waveform inversion (Chen *et al.*, 2013; Jaiswal *et al.*, 2008).

The near-surface community demonstrated that, in addition to the body-waves, Rayleigh waves can be used for near-surface soil characterization. Rayleigh waves can be inverted for shear-wave velocity (V_S) (Xia *et al.*, 1999; Xia *et al.*, 2000) with a caveat that the inversion process has a strong interpretation aspect and does not yield V_S directly (Beaty *et al.*, 2002; Brown *et al.*, 2000; Douma and Haney, 2011). Peer studies have also shown that S-refractions, which can be used to estimate V_S in the same way as their P-wave counterparts are used to estimate V_P, can be greatly beneficial for near-surface characterization. The inverted P- and S- refraction images can be combined as V_P/V_S ratio and Poisson's Ratio (σ) images, which can better resolve the near-surface than the individual V_P or V_S images. Notable examples include the works by King and Jarvis (2007) with their characterization of a polar firn and those by Bachrach *et al.* (2000) and

Ivanov *et al.* (2000), who characterized unconsolidated ground cover using the velocity ratios. King and Jarvis (2007) and Bachrach *et al.* (2000) estimated V_P and V_S, respectively, from analysis of first arrivals in vertical and horizontal geophones. In both these studies, the horizontal geophones were oriented perpendicular to the profile such that they are orthogonal to the P-ray vector and the first arrivals are pure horizontal shear (SH) mode of propagation. Here, I am referring to data acquired in such a manner as "tangential".

Ivanov *et al.* (2000) also obtained V_P from first arrival inversion of vertical-component data but used Rayleigh wave inversion to estimate V_S. All the above studies found that V_P/V_S or σ images can better resolve the near-surface than the individual V_P or V_S images. Till date no study is available that compared the traveltime resolution from orthogonal datasets to full-waveform resolution of a single component dataset. I am presenting this comparison in an ultrashallow setting by attempting to detect voids and pipes, speculating that they will be equally well resolved in the V_P/V_S ratio and/or σ images as the waveform images from V_P or V_S data.

On a related note, the V_S modeling has also been done by direct recording of the horizontal ground motion using three component (3C) phones. Applications of 3C data in near-surface investigation are not very common. Two representative case studies include Guevara et al. (2013) who used up-hole survey to compute near surface V_S and De Meersman (2013) who modeled both V_S and S-wave attenuation (Q_S^{-1}) within the weathering layer in Alberta. The recorded shear waves were dominantly mode-converted. Due to the layout of the phones with respect to the shots, the S-wave analysis first requires data rotation from the field to natural

coordinates, which, if not done properly, could be a significant source of amplitude errors. In this application I am not analyzing mode-converted reflections and therefore, not concerned with these processing steps.

1.3 CURRENT KNOWLEDGE GAP

Estimating strength and rock properties such as porosity and permeability of the near surface is a challenge. With seismic data, generally the surface wave inversion (MASW) method is used. The surface wave analysis is essentially the analysis of dispersion (different frequencies moving at different velocities), yields an approximate estimation of V_S. Although widely successful, it only reveals half of the information. Laboratory tests also do not necessarily replicate the field conditions and yield unbiased results because of the loose nature of sediments (porosity as much as 90%) and dry versus wet in-situ conditions.

In the Full Waveform Inversion (FWI), we used visco-acoustic approximation of the wave fields. Estimation of surface wave is beyond the scope of the visco-acoustic modeling. That is why it was crucial to remove the surface waves from the seismic data and analyze for body waves. I used two approaches of surface wave removal. First, I applied a simple bottom mute at the surface wave cone. Second, I used Redundant Lifting Scheme (RLS), which is a wavelet transform method (Aghayan and Jaiswal, 2016). RLS operates on trace-by-trace decomposition for each time series into wavelet coefficient (WC) time series and consequently a single gather (in a shot, receiver or CDP domain) into a series of WC sub-gathers. The advantage of RLS based coherent denoising method is that it has very minute effect on the lower end of the

frequency spectra. This is a valuable tool when data preconditioning is performed for advanced processing such as FWI, which benefits from desired low frequencies.

1.4 GOAL AND OBJECTIVES

The overarching goal of this project is to compare and contrast the applicability of traveltime versus full waveform inversion in ultra-shallow settings. The following three objectives will be accomplished:

i. Acquire vertical and tangential data over well documented and poorly documented targets,
ii. Perform traveltime and waveform inversion of the vertical and tangential data, and
iii. Prepare σ images from traveltime and waveform solutions.

Traveltime inversion is less intense computationally than that of FWI. In this research, I show that with properly designed acquisition, it is possible to characterize the near surface targets only with traveltime inversion. However, both vertical and tangential data are needed. Attenuation is also important in characterizing the subsurface, but it can only be achieved by full waveform inversion with computationally more intensive. Computation of attenuation may provide better conclusion of the modeling but this is solely flexible based on the project requirements. Here, I demonstrate that only traveltime inversion of vertical and tangential component seismic data is sufficient for near surface characterization if estimating attenuation is not necessary.

1.5 PROJECT SIGNIFICANCE AND BROADER IMPACTS

The study area represents a typical urban setting where utility pipes are buried below sodded field. Knowledge of physical property changes at such sites in the subsurface is critical for ensuring a safe and sustainable development. Seismic methods are sensitive to physical property changes and therefore should be routinely employed. However, imaging of elastic velocities in such areas is still a largely unexplored research topic due to unavailability of reliable modeling methods that can image the subsurface even in absence of reflection coda. In general models from stacking or migration velocity analysis may be too general for near surface purposes. Rapidly varying soil compaction, heterogeneous saturation which could have a seasonal variation and unexpected sources of anomalies (e.g., man-made objects from past construction or burial) are a few challenging considerations in near-surface interpretation.

The current research will best describe the near surface heterogeneity. It will provide a comparison of the utility of traveltime and full waveform inversion. This is going to be helpful in deciding which inversion methods to use in near surface studies at a certain scenarios. However, the velocity in shallow layers often varies considerably with location, which makes every near surface problem even more challenging. Although the method is demonstrated in an ultra-shallow target, it is applicable to other settings as well. For example, shear zone and zones of rupture have similar distortive qualities – fluid saturation varies rapidly and porosity could be very high (close to critical) in many parts. This will distort the waveforms beyond acoustic or elastic threshold. This idea may also be applicable to medical imaging, where fluids and pores

(in tissues and bones) distort waveform. However, designing experiments like this thesis in shear zones or medical imaging is very difficult.

1.6 REFERENCES

Al-Shuhail, A. A., and Adetunji, A., 2016, Joint Inversion of Ground-Penetrating Radar and Seismic Velocities for Porosity and Water Saturation in Shallow Sediments: Journal of Environmental and Engineering Geophysics, v. 21, no. 3, p. 105-119.

Bachrach, R., Dvorkin, J., and Nur, A. M., 2000, Seismic velocities and Poisson's ratio of shallow unconsolidated sands: Geophysics, v. 65, no. 2, p. 559-564.

Beaty, K., Schmitt, D., and Sacchi, M., 2002, Simulated annealing inversion of multimode Rayleigh wave dispersion curves for geological structure: Geophysical Journal International, v. 151, no. 2, p. 622-631.

Brown, L., Diehl, J. G., and Nigbor, R. L., A simplified procedure to measure average shear-wave velocity to a depth of 30 meters (VS30), *in* Proceedings Proceedings of 12th world conference on earthquake engineering2000.

Chen, J., Jaiswal, P., and Zelt, C. A., 2013, A case history: Application of frequency-dependent traveltime tomography and full waveform inversion to a known near-surface target, SEG Technical Program Expanded Abstracts 2013, p. 1743-1748.

De Meersman, K., 2013, S-waves and the near surface: A time-lapse study of S-wave velocity and attenuation in the weathering layer of an Alberta heavy oil field: The Leading Edge, v. 32, no. 1, p. 40-47.

Docherty, P., 1992, Solving for the thickness and velocity of the weathering layer using 2-D refraction tomography: Geophysics, v. 57, no. 10, p. 1307-1318.

Douma, H., and Haney, M., Surface-wave inversion for near-surface shear-wave velocity estimation at Coronation field, *in* Proceedings 81st SEG Annual Meeting2011, p. 1411-1415.

Francese, R., Giudici, M., Schmitt, D. R., and Zaja, A., 2005, Mapping the geometry of an aquifer system with a high-resolution reflection seismic profile: Geophysical Prospecting, v. 53, no. 6, p. 817-828.

Gallardo, L. A., and Meju, M. A., 2003, Characterization of heterogeneous near-surface materials by joint 2D inversion of dc resistivity and seismic data: Geophysical Research Letters, v. 30, no. 13.

Gallardo, L.A., and Meju, M.A., 2004, Joint two-dimensional DC resistivity and seismic travel time inversion with cross-gradients constraints: Journal of Geophysical Research: Solid Earth (1978–2012), v. 109, no. B3.

Guevara, S. E., Margrave, G. F., and Agudelo, W. M., 2013, Near-surface S-wave velocity from an uphole survey using explosive sources.

Ivanov, J., Park, C. B., Miller, R. D., and Xia, J., Mapping Poisson's ratio of unconsolidated materials from a joint analysis of surface-wave and refraction events, *in* Proceedings Proc. Symp. on the Application of Geophysics to Engineering and Environmental Problems (SAGEEP 2000), Arlington, Va2000, p. 11-17.

Jaiswal, P., Zelt, C. A., Bally, A. W., and Dasgupta, R., 2008, 2-D traveltime and waveform inversion for improved seismic imaging: Naga Thrust and Fold Belt, India: Geophysical Journal International, v. 173, no. 2, p. 642-658.

King, E. C., and Jarvis, E. P., 2007, Use of shear waves to measure Poisson's ratio in polar firn: Journal of Environmental & Engineering Geophysics, v. 12, no. 1, p. 15-21.

Lanz, E., Maurer, H., and Green, A. G., 1998, Refraction tomography over a buried waste disposal site: Geophysics, v. 63, no. 4, p. 1414-1433.

McBride, J. H., Stephenson, W. J., Williams, R. A., Odum, J. K., Worley, D. M., South, J. V., Brinkerhoff, A. R., Keach, R. W., and Okojie-Ayoro, A. O., 2010, Shallow subsurface structure of the Wasatch fault, Provo segment, Utah, from integrated compressional and shear-wave seismic reflection profiles with implications for fault structure and development: Geological Society of America Bulletin, v. 122, no. 11-12, p. 1800-1814.

Santamarina, J. C., Rinaldi, V. A., Fratta, D., Klein, K. A., Wang, Y.-H., Cho, G. C., and Cascante, G., 2005, A survey of elastic and electromagnetic properties of near-surface soils: Near-Surface Geophysics, v. 1, p. 71-87.

Williamson, P., 1991, A guide to the limits of resolution imposed by scattering in ray tomography: Geophysics, v. 56, no. 2, p. 202-207.

Xia, J., Miller, R. D., and Park, C. B., 1999, Estimation of near-surface shear-wave velocity by inversion of Rayleigh waves: Geophysics, v. 64, no. 3, p. 691-700.

Xia, J., Miller, R. D., Park, C. B., Hunter, J. A., and Harris, J. B., 2000, Comparing shear-wave velocity profiles from MASW with borehole measurements in unconsolidated sediments, Fraser River Delta, BC, Canada: Journal of Environmental & Engineering Geophysics, v. 5, no. 3, p. 1-13.

Zelt, C. A., Azaria, A., and Levander, A., 2006, 3D seismic refraction traveltime tomography at a groundwater contamination site: Geophysics, v. 71, no. 5, p. H67-H78.

Zhang, J., and Toksöz, M., 1998, Nonlinear refraction traveltime tomography: GEOPHYSICS, v. 63, no. 5, p. 1726-1737.

PAPER I

NEAR SURFACE CHARACTERIZATION USING V_P/V_S AND POISSON'S RATIO FROM SEISMIC REFRACTIONS

2.1 ABSTRACT

This paper shows that the ratio of compressional– and shear–wave velocities (V_P and V_S, respectively) better characterizes the near-surface than individual velocity models. In a proof-of-concept experiment, vertical and tangential data were acquired along a 23 m, 2D profile containing two well-documented utility pipes with 0.76 m diameter and 1.5 m burial depth. First arrivals of both datasets were inverted using a regularized tomography algorithm. The inverted V_P and V_S images, which fit their respective datasets within the noise level, were smooth with no clear anomalous structure at the pipe locations. In the V_P/V_S ratio image, however, the pipe locations appear as zones with high ratio values (>1.8). A nearby zone of low (<1.5) V_P/V_S ratio was interpreted as a backfilled void. These results suggested that carefully conducted P-and S-refraction tomography can provide quick and effective near-surface reconnaissance.

2.2 INTRODUCTION

The top few meters of the earth is a zone of interaction among the atmosphere, biosphere, and hydrosphere that sustains the majority of anthropogenic activities. Therefore, its soil properties, including porosity, density, bulk and shear moduli are of great interest to many communities, such as those that focus on the environment, engineering, and archeology (Bement *et al.*, 2007; Goodman, 1994; Sharma, 1997; Wright and Duncan, 2005). In laboratory settings, Santamarina *et al.* (2005) showed that subtle changes in soil properties, such as porosity, particle dimension, pore-fluid type, and saturation, could significantly alter their elastic response, implying that the seismic velocities can be a valuable tool for near-surface characterization. However, estimating velocities accurately with sufficient resolution in the near surface is a challenge. Particularly in the upper tens of meters, where newly deposited or eroded material often lacks compaction and stratification required for generating reflections, velocity estimation is difficult. Building velocity models with methods, such as normal move-out (Al-Yahya, 1989), that are frequently used in basin-scale studies is inappropriate in the near-surface.

In field settings, refraction studies are generally conducted with vertical-component datasets for creating P-wave velocity (V_P) models. Traditionally, refraction studies have been used for detection of the base of the weathered layer (Docherty, 1992; Lanz *et al.*, 1998) and addressing similar problems, but a limited number of studies have also shown that refractions can also be used to infer porosity and stiffness of the soil (Francese *et al.*, 2005; McBride *et al.*, 2010; Zelt *et al.*, 2006; Al-Shuhail and Adetunji, 2016). Refraction resolution is typically defined by the order of the radius of the first Fresnel Zone (Williamson, 1991; Zhang and Toksöz, 1998), and we expand upon this in the Appendix. Therefore, for smaller targets, the refraction models have to

be refined using other, more advanced methods such as jointly with resistivity (Gallardo and Meju, 2003, 2004) and full-waveform inversion (Chen *et al.*, 2013; Jaiswal *et al.*, 2008).

The near-surface community has shown that, in addition to the body-waves, Rayleigh waves can be used for near-surface soil characterization. Rayleigh waves can be inverted for shear-wave velocity (V_S) (Xia *et al.*, 1999; Xia *et al.*, 2000) with a caveat that the inversion process has a strong interpretation aspect and does not yield V_S directly (Beaty *et al.*, 2002; Brown *et al.*, 2000; Douma and Haney, 2011). Peer studies have also shown that S-refractions, which can be used to estimate V_S in the same way as their P-wave counterparts are used to estimate V_P, can be greatly beneficial for near-surface characterization. The inverted P- and S- refraction images can be combined as V_P/V_S ratio and Poisson's Ratio (σ) images, which can better resolve the near-surface than the individual V_P or V_S images. Notable examples include the works by King and Jarvis (2007) with their characterization of a polar firn and those by Bachrach *et al.* (2000) and Ivanov *et al.* (2000), who characterized unconsolidated ground cover using the velocity ratios. King and Jarvis (2007) and Bachrach *et al.* (2000) estimated V_P and V_S, respectively, from analysis of first arrivals in vertical and horizontal geophones. In both these studies, the horizontal geophones were oriented perpendicular to the profile such that they are orthogonal to the P-ray vector and the first arrivals are pure horizontal shear (SH) mode of propagation. Hereafter, we refer to data acquired in such a manner as "tangential". Ivanov *et al.* (2000) also obtained V_P from first arrival inversion of vertical-component data but used Rayleigh wave inversion to estimate V_S. All the above studies found that V_P/V_S or σ images can better resolve the near-surface than the individual V_P or V_S images. In this paper, we extend the idea to detect voids and

pipes in the near surface, speculating that they will be better resolved in the V_P/V_S ratio and σ images, which can better resolve the near-surface than the individual V_P or V_S images.

Our study area is located at Oklahoma State University's main campus (Fig. 1), which is typical of an urban setting with a number of utility pipes and excavations below the ground cover, not all of which are well-documented. To test how well refractions can characterize these artifacts, we acquired vertical and tangential datasets along a 2D profile containing two well-documented utility pipes (Fig. 1), both are 0.76 m in diameter and located approximately at the central part of the survey with 1.5 m burial depth. A poorly-documented backfilled area, which is the old location of one of the utility pipes, is also expected towards the west end of the profile. The soil type at the test site is unsaturated to partially saturated sandy clay. We have organized the paper as follows: first, we outline the seismic survey parameters, present the data, and show first arrival picks. Following this, we briefly describe the regularized tomography methodology and invert the first arrival times for obtaining V_P and V_S images. Then, we assess the resolution of the images. Finally, we examine which form of output is best for resolving the pipes –individual velocity images or their ratios.

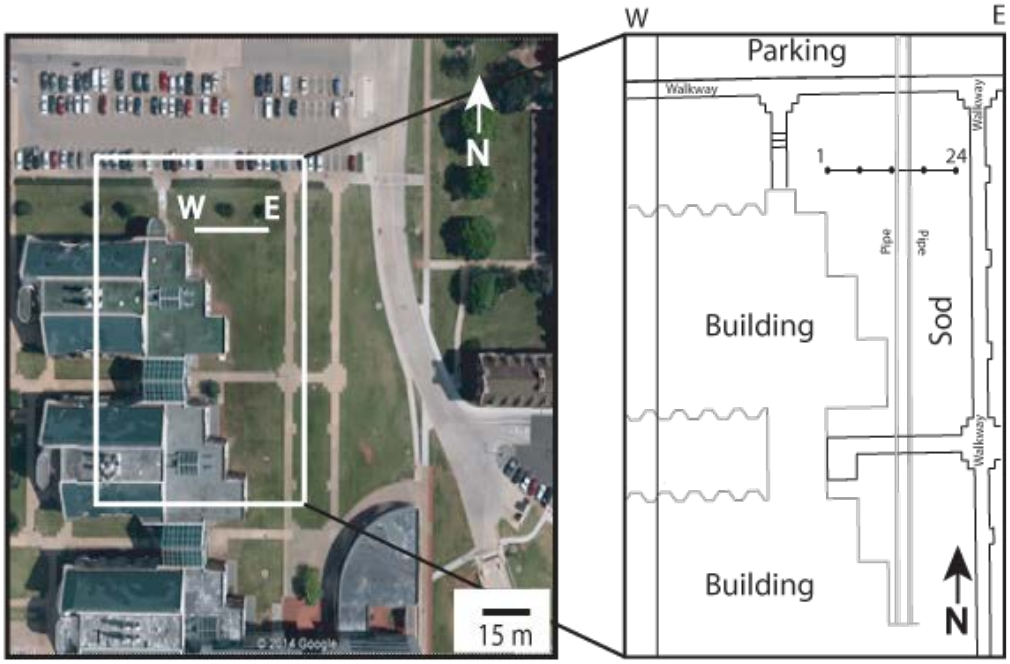

Figure 1: Google Earth image of Oklahoma State University's Main Campus. The study area is shown with a white box. An enlarged sketch showing the seismic profile, utility pipes as well as a few key campus landmarks is also presented.

2.3 SURVEY AND DATA

We collected vertical and tangential datasets along a common 23 m east-west 2D profile orthogonal to the plumbing system in two separate acquisitions, using a static array of 24 geophones spaced 1m apart (Fig. 1). For the vertical dataset, we used 40 Hz vertical geophones and fired the shots at every geophone location. For the tangential dataset, we used 28 Hz horizontal geophones and fired the shots in between the geophones to avoid the existing shot holes. The sources in both cases were point explosives, *i.e.*, 12–gauge 400–grain shells fired from a shotgun (Betsy Seisgun) set off in 15 cm-deep holes noting that both P- and S- modes

propagation can be generated from a point source (Fertig, 1984; Geyer and Martner, 1969). Both datasets were recorded using 24-channel Geometrics-Geode seismographs. Sample interval and recording length for both datasets were 0.125 ms and 500 ms, respectively. The vertical and horizontal datasets had dominant frequencies of approximately 100 Hz and 60 Hz, respectively. The vertical and tangential datasets had 24 and 23 shot gathers, respectively. The near and far offsets for the vertical dataset were 0 and 23 m, and for the tangential dataset were 0.5 m and 22.5 m, respectively. To avoid instrument oscillations, the horizontal geophones were buried under 15 cm of soil. The survey was designed such that the documented utility pipes were in the middle of the profile.

The vertical and tangential datasets comprised 576 and 552 traces, respectively. Overall, the tangential dataset was noisier than the vertical dataset but the first arrivals could be picked in both datasets, up to the maximum source-receiver separation (Fig. 2). In both datasets, the first arrival time generally increases with source-receiver separation (Fig. 3(a) and (b)) and a difference plot is shown as the tangential minus the vertical dataset (Fig. 3(c)). In either dataset, we could not identify any reflections or diffractions that would be indicative of shallow mode-converting horizons. We could also identify the surface wave cones in both datasets (Fig. 2). Therefore, we assumed that, much like in the peer studies, the leading waveforms in the vertical and tangential datasets are exclusive records of P- and SH- propagation modes.

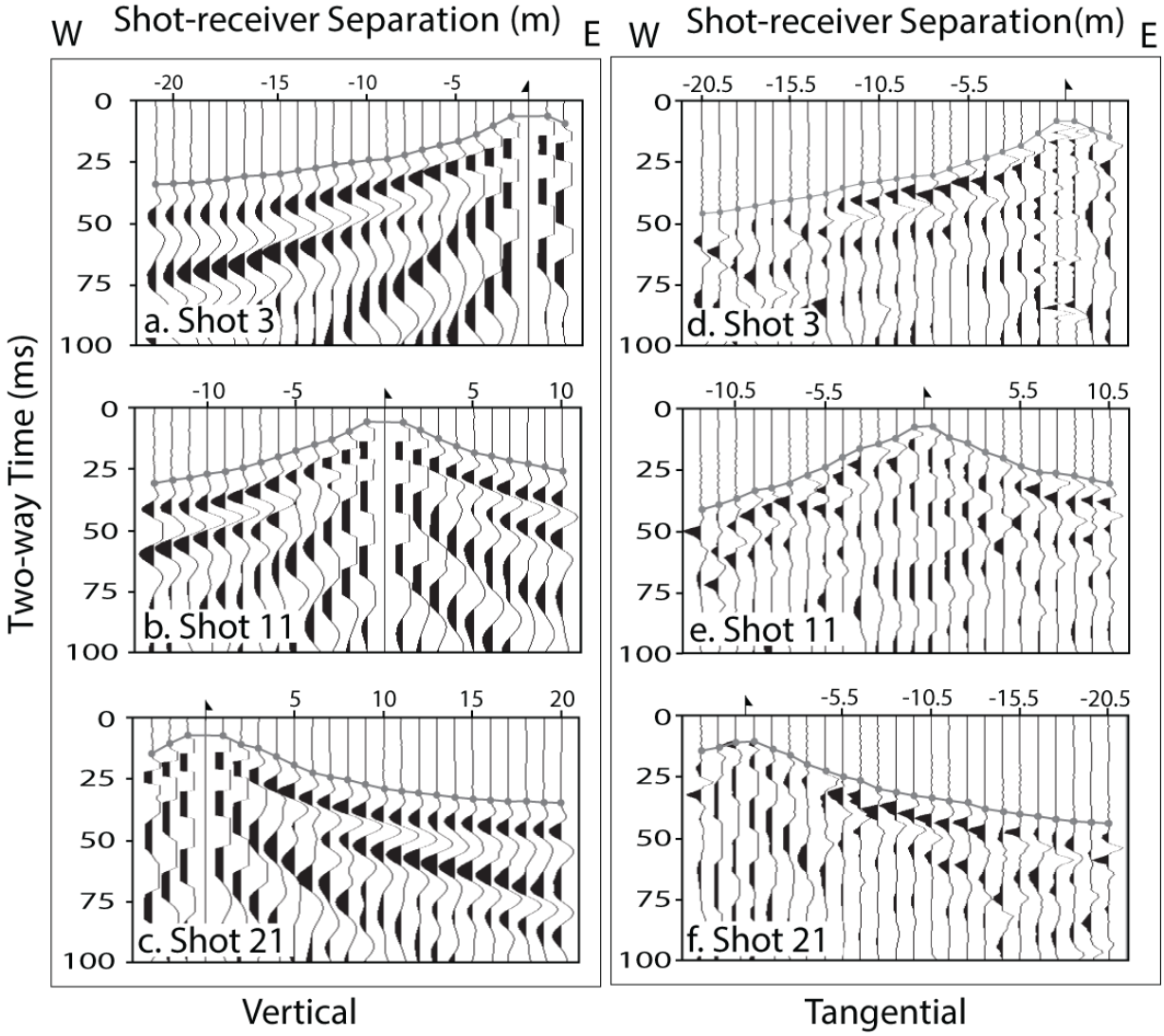

Figure 2: Representative data. a) – c) Vertical component and d) – f) Tangential component gathers for shots 3, 11, and 21. The flags and dots represent shot locations and the first arrival times, respectively.

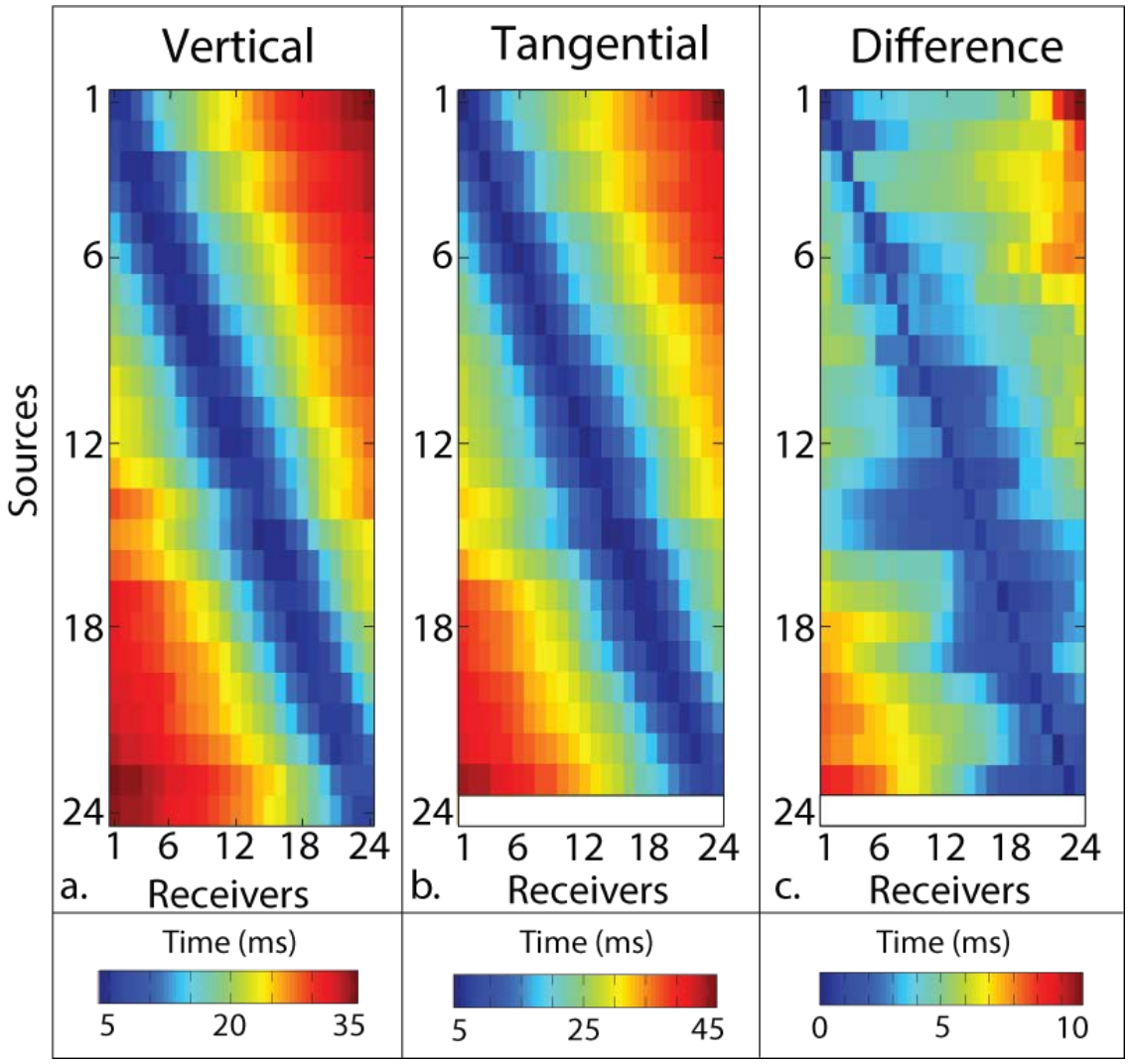

Figure 3: First-arrival times. a) Vertical, b) Tangential, c) Difference (Tangential minus Vertical). In a) through c) light to dark gradation represents arrival times ranging from near- to far- source-receiver separation. The arrival times follow a diagonal pattern as shot moves from one end to the other end of the profile.

2.4 METHODS

2.4.1 TRAVELTIME INVERSION

Our traveltime inversion is based on the regularized Zelt and Barton (1998) method. We present a summary of the method below and guide the reader to the original reference for details. Traveltime inversion searches for a solution that fits the observed arrival times within a predetermined uncertainty. An initial velocity model is created which is then updated iteratively using misfit between the observed and predicted travel times. The forward modeling in this method is implemented on a finite-difference grid. The method solves the eikonal equation (Eq. 1) modified to handle large velocity variations after Hole and Zelt (1995):

$$\nabla t \cdot \nabla t = \left|\nabla t\right|^2 = \frac{1}{c^2} \quad , \qquad (1)$$

where c^{-1} is the slowness, ∇t is the delay time, such that $c\nabla t$ is a unit vector in the direction of the ray.

The inverse problem satisfies a convergence criterion by minimizing an objective function, *E(m)*, which is the L_2 norm of a combination of data errors and model roughness (Eq. 2):

$$E(m) = \Delta d^T C_d^{-1} \Delta d + \lambda [m^T C_h^{-1} m + s_z m^T C_v^{-1} m] \qquad (2)$$

In Equation 2, m is a model vector, Δd is the difference between d_{pre} and $d_{obs,}$ (d_{pre} is the predicted and d_{obs} is the observed data vector), C_d is the data covariance matrix, C_h and C_v are model space covariance matrices that measure horizontal and vertical roughness respectively, λ

is the trade-off parameter, and s_z determines the relative importance of maintaining vertical versus horizontal model smoothness.

In general, if m^k is the model in the k^{th} iteration, δm is defined as the model perturbation such that $m^{k+1} = m^k + \delta m$. The value for δm is computed using the jumping strategy of Shaw and Orcutt (1985) (Eq. 3). Regularization in the Zelt and Barton (1998) method, implemented by scaling with the inverses of the data and model space covariance matrices, attempts to obtain the smoothest model appropriate for the data errors (Scales et al., 1990). The stopping criterion for traveltime inversion is based on a user-defined range of data uncertainty of the observed data.

$$\begin{bmatrix} C_d^{-\frac{1}{2}} L \\ \lambda C_h \\ s_z \lambda C_v \end{bmatrix} \delta m = \begin{bmatrix} C_d^{-\frac{1}{2}} L \\ -\lambda C_h m_k \\ -s_z \lambda C_v m_k \end{bmatrix} \qquad (3)$$

In Eq. 3, L is the partial derivative matrix of the data errors with respect to the model parameters.

2.4.2 POISSON'S RATIO:

The σ is a measurement of the shrinkage of a material in the direction orthogonal to the direction of tensile stress. Mathematically, it is defined as the ratio of latitudinal to longitudinal strain. In most cases, σ varies between 0 and 0.5, with higher σ indicating a rubber-like material which can be easily sheared and lower σ indicating that the material is increasingly resistant to shearing. In terms of velocity ratios, $v = V_P/V_S$, σ can be expressed as:

$$\sigma = 0.5\frac{\nu^2 - 2}{\nu^2 - 1} \quad (4)$$

2.5 MODELING AND RESULTS

For traveltime inversion, 576 and 552 first-arrival times were picked in the vertical and tangential datasets, respectively (Fig. 2). Based on the dominant frequency and the level of ambient noise, 1 ms and 2 ms uncertainties were respectively assigned to the vertical and horizontal datasets. Starting models for both datasets were 1D in nature, where velocities increased linearly with depth. For the vertical dataset, V_P increases from 200 m/s at the surface to 1800 m/s at 20 m depth and for the tangential dataset, V_S increases from 100 m/s at the surface to 1200 m/s at 20 m depth. These gradients are not arbitrary and were determined heuristically through repeated inversion runs. After every inversion, the final image was averaged to create the starting model for the next inversion. Using these 1D background models, the inversion for vertical and tangential datasets converged in 9 and 13 iterations, respectively. Notably traveltimes were fit to within their assigned uncertainties of 1 ms and 2 ms for the vertical and tangential components, respectively.

The final V_P and V_S images (Fig. 4(a) and (b), respectively) have a smooth structure with no clear indications of any anomalous zones that can be related to the utility pipes. However, when presented in terms of perturbations, *i.e.*, percentage change from the starting model as shown in Figs. 5(a) and (b), V_P and V_S updates at the target zones appear to be better resolved. In Fig. 5(a), the pipe at the 13 m distance (western pipe) manifests as the zone of ~5% V_P increase but the

pipe at the 16.5 m distance (eastern pipe) is not well resolved. In Fig. 5(b), on the other hand, the western pipe is not resolved but the eastern pipe manifests as a zone of ~2.5% V_S decrease. In Fig. 5(a), at 8 m distance and 2.5 m below the surface, there is a zone with ~5% velocity decrease that is interpreted as a backfilled void. This anomaly is at the approximate location of a poorly-documented location of a previous utility pipe. In Fig. 5(b), this backfilled void is associated with a ~1% velocity decrease. Both V_P and V_S changes associated with the pipe locations are subtle (Figs. 5(a) and (b), respectively) and therefore a thorough assessment of the solution is needed.

First, we assess the solution through ray-count plots (Figs. 6(a) and 6(b) for V_P and V_S images, respectively). In these figures, ray coverages do not appear to be abnormally high or low at the target locations as compared to the background, implying that the velocity updates in Figs. 5(a) and 5(b) are not biased. Next, we assess the solution through the checkerboard test, which is a common form of nonlinear assessment of tomographic solutions (Day *et al.*, 2001; Evangelidis *et al.*, 2004). Checkerboard tests are synthetic tests where artificially induced alternating highs and lows in a background velocity model is reconstructed in the same manner as with the real data (Lévěque *et al.*, 1993; Rawlinson and Spakman, 2016). Although initially developed for crustal-scale problems, Zelt *et al.* (2006) showed that checkerboard tests are valuable in near-surface scenarios as well.

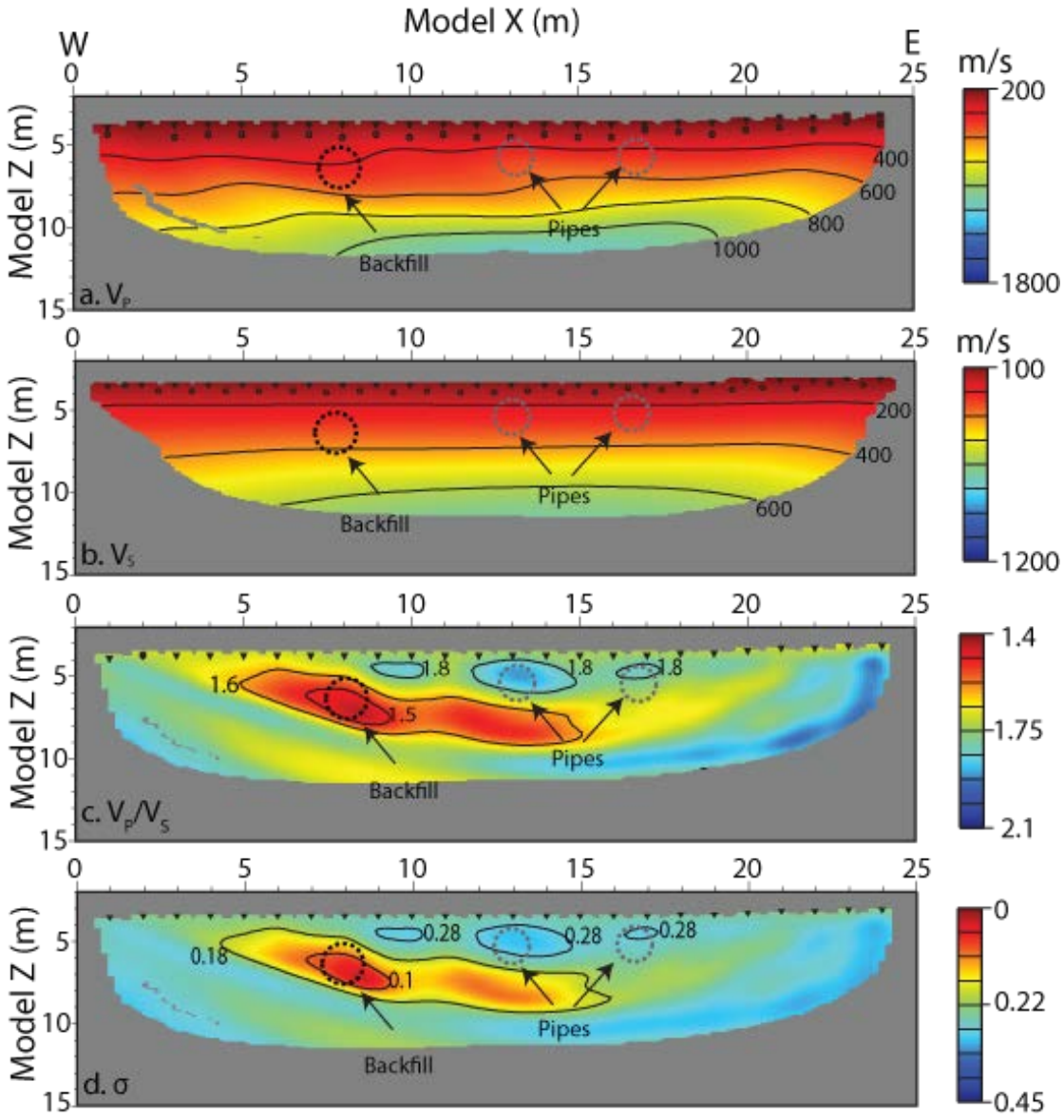

Figure 4: Final inverted images. a) V_P, b) V_S, c) V_P/V_S , and d) σ. Gray dotted ellipses show the locations of utility pipes, black dotted ellipse shows the location of the backfilled void, black triangles represent the receiver positions and open black circles represent source locations. In a) and b) no updates below the ray coverage are shown. Figure indicates that the utility pipes are better resolved in c) and d) compared to a) and b). The V_P and V_S models have been generated with 1 ms and 2 ms pick uncertainties, respectively.

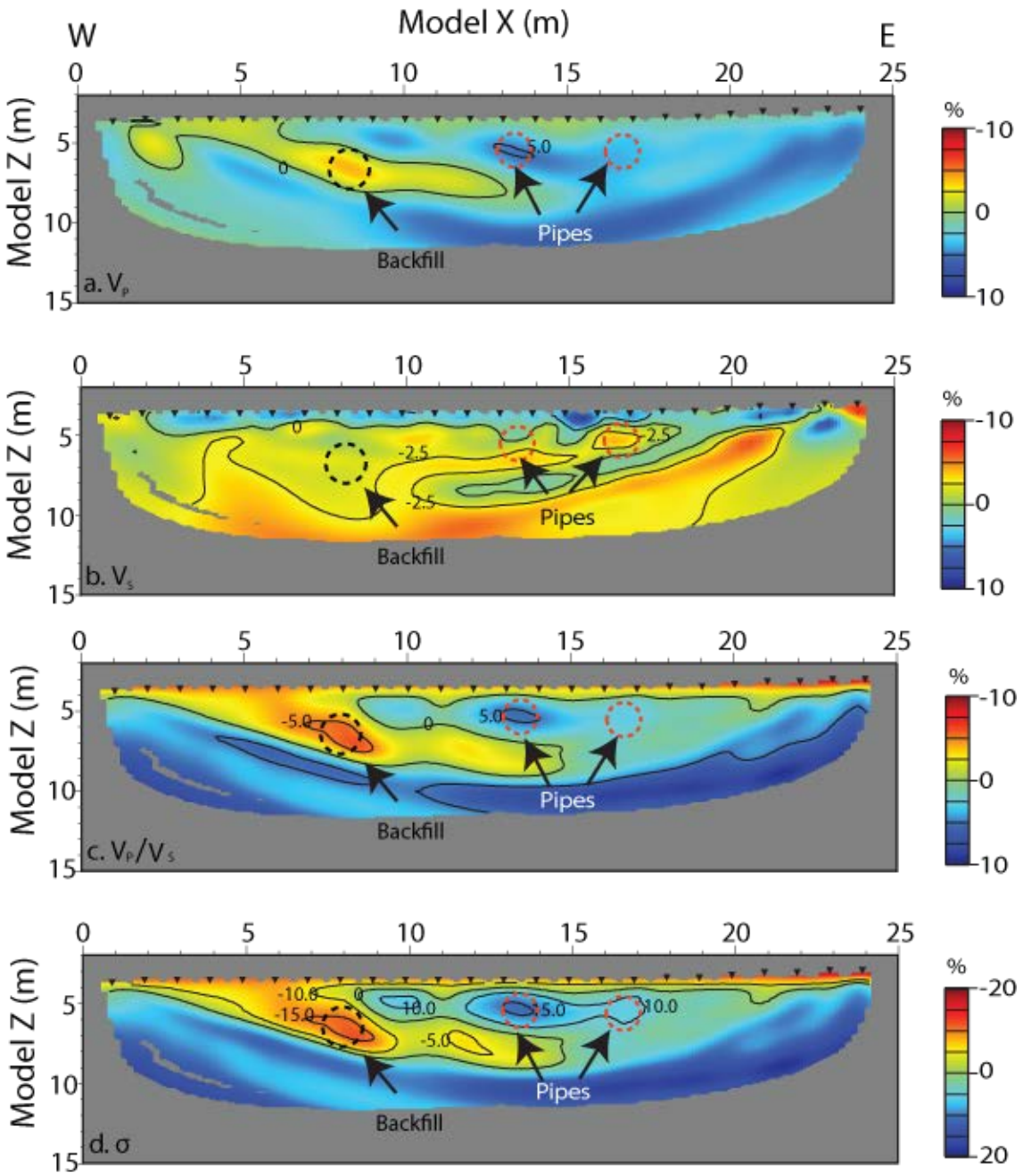

Figure 5: Final updates from stating models. a) V_P, b) V_S, c) V_P/V_S, and d) σ. Symbols have the same meaning as in Fig. 4. Note that only the western pipe is resolved in a) and only the eastern pipe is resolved in b). Figure indicates that the utility pipes are better resolved in c) and d) compared to a) and b).

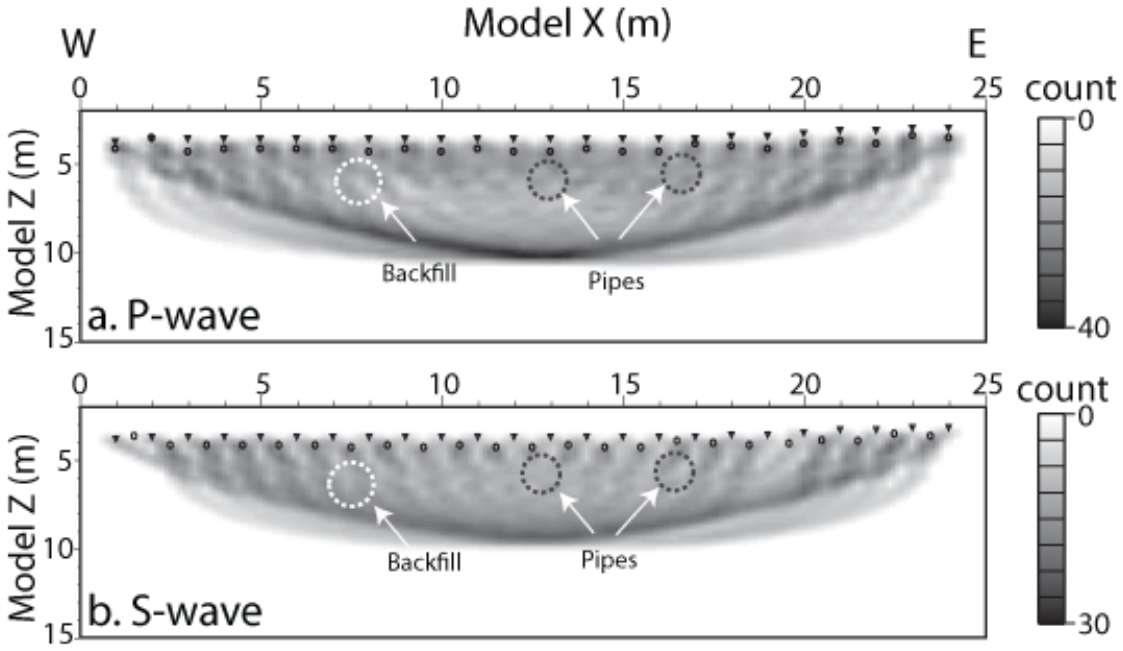

Figure 6: Ray count plots. (a) P-wave and (b) S-wave. Symbols have the same meaning as in Fig. 4. Figure does not indicate abnormal ray coverage at the targets.

For the checkerboard test, we perturb the 1D background V_P and V_S models in a checkerboard grid of sizes 0.5 m, 0.75 m, 1 m and 1.5 m and a peak strength of ±5% (Fig. 7). In every scenario, we simulate the traveltime from the perturbed model and invert the simulated traveltimes using the 1D background model as the starting model. Much like their unperturbed counterparts, we assign 1 ms of uncertainty to V_P datasets and 2 ms of uncertainty to V_S datasets respectively. The results show that the 0.5 m and 0.75 m grid sizes are not well resolved in either the inverted V_P or V_S images (Figs. 7(a), 7(b) and 7(e), 7(f), respectively). Both polarity and the peak amplitude of the 1 m grid size are well-resolved at the target depths in the inverted V_P image (Fig. 7(c)). However, in the inverted V_S image, only the polarity of the 1 m grid is

properly recovered at the target depths (Fig. 7(g)). The maximum recovered magnitude is approximately 2.5% (grids points between 10 m and 15 m model distance), whereas the initial perturbation as an input was ±5%. We note that the recovery of the 1 m grid is very similar to inversion results of real data in Figs. 5(a) and 5(b). Overall and as nominally expected, larger grids are better resolved in Fig. 7.

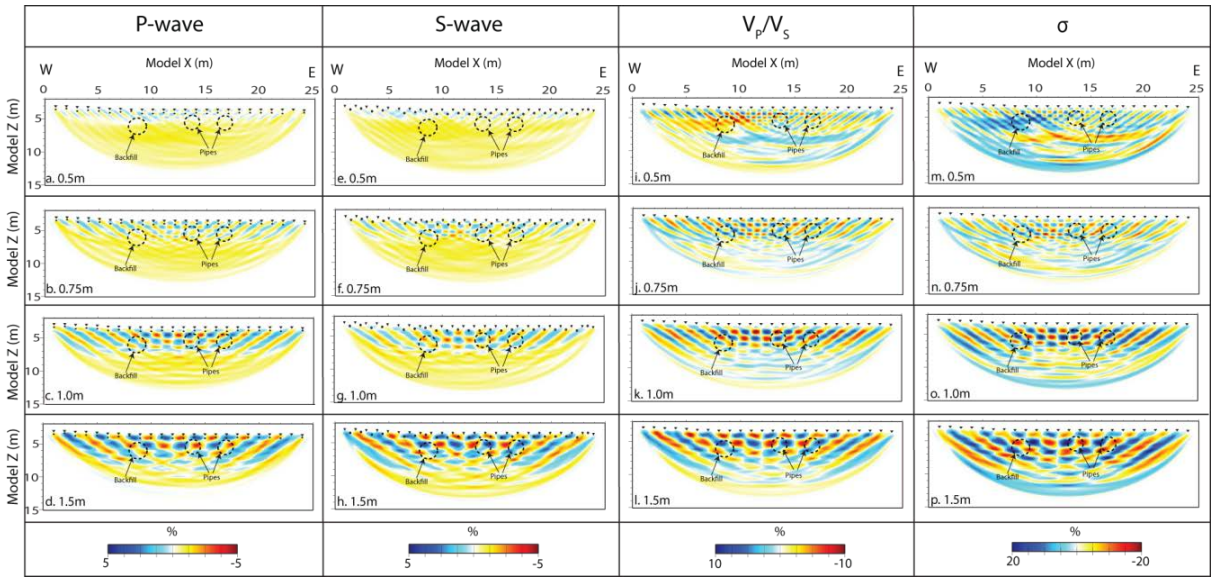

Figure 7: Checkerboard tests. V_P perturbation recovered for a) 0.5 m, b) 0.75 m, c) 1 m and d) 1.5 m grid sizes. V_S perturbation recovered for e) 0.5 m, f) 0.75 m, g) 1 m and h) 1.5 m grid sizes. V_P/V_S ratio of recovered perturbations for i) 0.5 m, j) 0.75 m, k) 1 m and l) 1.5 m grid sizes. Possion's Ratio (σ) of recovered perturbations for m) 0.5 m, n) 0.75 m, o) 1 m and p) 1.5 m grid sizes. The V_P and V_S models have been generated with 1 ms and 2 ms pick uncertainties respectively. Symbols have the same meaning as Fig. 4. Figure suggests that resolution of the V_P/V_S ratio and σ is better than the individual velocity images.

Figures 7(i) through 7(l) and 7(m) through 7(p) are the V_P/V_S and σ images generated from the inverted V_P and V_S checkerboard images. It is notable that for all scenarios (0.5 m, 0.75 m, 1.0 m and 1.5 m grids) the checkerboard polarity and shapes are better expressed in the V_P/V_S ratio and σ images as compared to individual velocity images of Figs. 7(a) through 7(d) and 7(e) through 7(h). This is an important finding as it provides motivation for generating V_P/V_S and σ images for interpreting the real data. On a related note, the central part of the V_P/V_S and σ images are better resolved in terms of shape and magnitude compared to the edges, where the recovered perturbations are smeared. Further, as the grid sizes increase from 0.5 m to 1.5 m, the extent of the well-resolved zone also increases, which is probably reflective of the frequency bandwidth used in the inversion. Checkerboard results in Fig. 7 are also consistent with the Fresnel Zone criteria, as demonstrated in the Appendix.

Next, we generated V_P/V_S and σ images using the inverted images from Figs. 4(a) and 4(b). We find that, overall, the V_P/V_S ratio ranges between 1.4 and 2.1 (Fig. 4(c)), the background has a V_P/V_S ratio of ~1.6, the zones containing the two utility pipes have a higher V_P/V_S ratio (>1.8), and the backfilled zone has a lower V_P/V_S ratio (<1.5). We observe similar structure in the σ image (Fig. 4(d)). Overall, σ of the background soil ranges between 0.2 and 0.3, which is consistent with Sharma *et al.* (1990) for similar sediment type. The zone with the utility pipes have higher-than-background σ (>0.28 vs. ~0.2) and the backfilled zone has lower-than-background σ (<0.1 vs. ~0.2). Clearly, the targets are better resolved in the V_P/V_S (Fig. 4(c)) and the σ (Fig. 4(d)) images than in the individual inverted velocity images.

2.6 DISCUSSION

In general, because S-waves travel more slowly than P-waves, they are expected to yield a higher resolution. In our case, lower S-wave resolution is observed than P-wave, which warrants an explanation. In tomography, images are intentionally kept smooth to avoid over-interpretation. Discounting geological factors, image smoothness depends on the offset structure of the picks *i.e.*, the spatial pattern of the arrival times as a function of source-receiver separation. Statics, or traveltime variations associated with the shallow structures or topography, can therefore result in noisier images. Statics are generally addressed by assigning higher uncertainty to the time picks, which unfortunately restricts image recovery to larger wavelength features. In our case, the S-wave geophones were buried under 15 cm of soil. Although this was a crucial step to avoid the instrument oscillation, we speculate that it may have incorporated some static variations in the data. A generalized reciprocal analysis, *i.e.*, comparing arrival times when the source and receivers switch locations, suggested that pick uncertainty of less than 2 ms was not reasonable for the tangential dataset. Thus, it is believed that resolution of the tangential data were poor because of a higher pick uncertainty. The uncertainty could not be reduced; otherwise the model would have become excessively noisy. Resolution tests can be used to understand this phenomenon. In Fig. 8(a), the inverted V_P image for the recovered 1 m checkerboard grid size (same as Fig. 7(c)) is shown. In Figs. 8(b) and 8(c) the inverted V_S images recovered using 2 ms and 1 ms pick uncertainties are shown. As expected, image resolution in Fig. 8(c) is comparable to Fig. 8(a). Figure 8 implies that if the tangential dataset was as "clean" as its vertical counterpart, the resolution of the V_S image could have been as good as the V_P image. This, however, does not necessarily imply that the western pipe would also have been resolved in the V_S image.

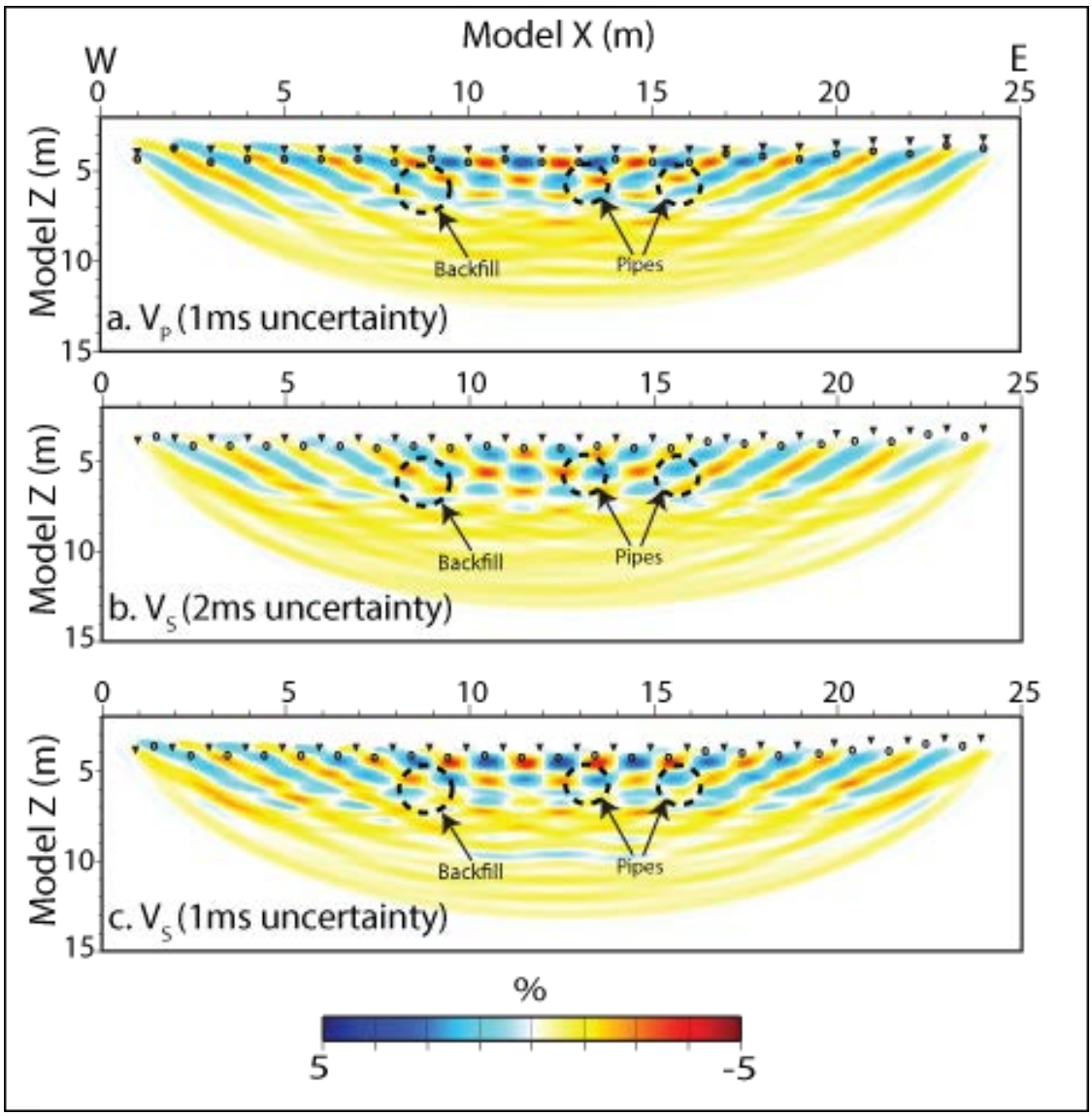

Figure 8: Pick uncertainty and model resolution. a) 1 m V_P checkerboard recovered using with 1 ms uncertainty, b) 1 m V_S checkerboard recovered using with 2 ms uncertainty and c) 1 m V_S checkerboard recovered using with 1 ms uncertainty. In a) through c), the checkerboards were created with 5% perturbation. Symbols have the same meaning as in Fig. 4. Figure suggests that tangential and vertical datasets will have similar resolution if data uncertainties are comparable.

It is notable in Figs. 5(a) and 5(b) that the western pipe is poorly resolved in the V_S image and the eastern pipe is poorly resolved in the V_P image. Yet, the V_P/V_S and σ images resolve both pipes (Figs. 4(c) and 4(d)). These results can be appreciated through the relative V_P/V_S and σ perturbation (Figs. 5(c) and (d)). Let us assume a background V_P and V_S of 400 m/s and 240 m/s, similar to the model, 1 m below the surface. These values correspond to a V_P/V_S ratio of 1.667 and σ of 0.21. For a 5% increase in the V_P and 1% decrease in the V_S, *e.g.*, at the utility pipe located at 12 m image distance, the V_P/V_S ratio increases by 6%. The ratio increase is still comparable to the V_P update, but the σ increases by 20% and is an order of magnitude larger than the change in V_P. Similarly, when V_P decreases by 5% and V_S decreases by 2%, *e.g.*, at the backfilled void, the V_P/V_S ratio decreases by 3%. The ratio decrease is actually smaller than the V_P change, but the σ decreases by 13% and is significant. The expression of σ magnifies even the most subtle change in V_P or the V_S. We acknowledge the risk that inversion artifacts may also become magnified in σ images and therefore emphasize on the need of careful interpretation. In summary, because the V_P/V_S and σ models have contributions from both V_P and V_S models, they provide a more complete near-surface description.

On a related note, it is not clear why the western and eastern pipes are selectively resolved in the V_P and V_S images. Both pipes are identical in composition therefore their velocity behaviors must originate from the soil that locally hosts the pipe. Difference in factors such as compaction, saturation, composition, porosity and sorting could have led to these observations (Santamarina *et al.*, 2005). We also remind the reader that the resolution achieved at the target level is reflective of the bulk properties of essentially a 1 m zone comprising the utility pipe and the surrounding soil.

Our results also show the presence of other anomalous zones in the images. For example, a zone of high V_P/V_S ratio (>1.8) is observed about 10 m image distance and ~1.5 m image depth. To the best of our knowledge, there is no documentation of this location being associated with any utility pipes. This zone lies immediately above the backfilled void and therefore the increase in V_P/V_S ratio could have resulted from compaction that followed the backfilling process. However, it could also be another, undocumented, utility pipe. It is difficult to distinguish between the two scenarios based only on the seismic method. Other geophysical tools such as resistivity profiling could be used to augment our results.

2.7 CONCLUSIONS

To test the idea that V_P/V_S and σ images have better resolution than individual inverted V_P and V_S images, a ground-truthing refraction experiment was conducted along a 23 m long profile where two utility pipes were documented and a backfilled void was suspected. Assuming that leading waveforms in vertical and tangential datasets are P- and SH- propagation modes, V_P and V_S images were created using first-arrival tomography. Results showed that the western pipe was not resolved in the V_S image while the eastern pipe was not resolved in the V_P image, but both pipes were resolved in the V_P/V_S ratio and σ images. Within the background sediments of ~0.2 σ, the pipes and the backfilled void manifested as high (>0.28) and low (<0.1) σ zones. This paper suggests that carefully acquired P-and S-refractions could be analyzed for a quick and effective reconnaissance of the near surface.

2.8 ACKNOWLEDGEMENTS

The paper would not have reached its present shape without the suggestions of William Doll, two anonymous reviewers, and the editor, Dale Rucker. We gratefully acknowledge their efforts. Besides the authors, the data acquisition team comprised Salman Abbasi, Khemraj Shukla, Pouyan Ebrahimi, Brooke Briand and Emily Guderian. The Physical Plant at Oklahoma State University provided the blueprint and scoped the problem. The Oklahoma State University Geophysical Society student chapter partially funded the survey. This is the Boone Pickens School of Geology, Oklahoma State University, contribution number: 2016-38.

2.9 REFERENCES

Al-Shuhail, A.A., and Adetunji, A., 2016, Joint Inversion of Ground-Penetrating Radar and Seismic Velocities for Porosity and Water Saturation in Shallow Sediments: Journal of Environmental & Engineering Geophysics, **21**, 105-119.

Al-Yahya, K., 1989, Velocity analysis by iterative profile migration: Geophysics, **54**, 718-729.

Bachrach, R., Dvorkin, J., and Nur, A.M., 2000, Seismic velocities and Poisson's ratio of shallow unconsolidated sands: Geophysics, **65**, 559-564.

Beaty, K., Schmitt, D., and Sacchi, M., 2002, Simulated annealing inversion of multimode Rayleigh wave dispersion curves for geological structure: Geophysical Journal International, **151**, 622-631.

Bement, L.C., Carter, B. J., Varney, R.A., Cummings, L. S., and Sudbury, J. B., 2007, Paleo-environmental reconstruction and bio-stratigraphy, Oklahoma Panhandle, USA: Quaternary International, **169–170**, 39-50.

Brown, L., Diehl, J.G., and Nigbor, R.L., 2000, A simplified procedure to measure average shear-wave velocity to a depth of 30 meters (VS30): in Proceedings of 12th world conference on earthquake engineering, p. 1-8.

Chen, J., Jaiswal, P., and Zelt, C.A., 2013, A case history: Application of frequency-dependent traveltime tomography and full waveform inversion to a known near-surface target: SEG Technical Program Expanded Abstracts 2013, p. 1743-1748.

Day, A.J., Peirce, C., and Sinha, M.C., 2001, Three-dimensional crustal structure and magma chamber geometry at the intermediate-spreading, back-arc Valu Fa Ridge, Lau Basin—results of a wide-angle seismic tomographic inversion: Geophysical Journal International, **146**, 31-52.

Docherty, P., 1992, Solving for the thickness and velocity of the weathering layer using 2-D refraction tomography: Geophysics, **57**, 1307-1318.

Douma, H., and Haney, M., 2011, Surface-wave inversion for near-surface shear-wave velocity estimation at Coronation field: SEG Technical Program Expanded Abstracts 2011, p. 1411-1415.

Evangelidis, C., Minshull, T., and Henstock, T., 2004, Three-dimensional crustal structure of Ascension Island from active source seismic tomography: Geophysical Journal International, **159**, 311-325.

Fertig, J., 1984, Shear waves by an explosive point-source: the earth surface as a generator of converted PS waves: Geophysical Prospecting, **32**, 1-17.

Francese, R., Giudici, M., Schmitt, D.R., and Zaja, A., 2005, Mapping the geometry of an aquifer system with a high-resolution reflection seismic profile: Geophysical Prospecting, **53**, 817-828.

Gallardo, L.A., and Meju, M.A., 2003, Characterization of heterogeneous near-surface materials by joint 2D inversion of dc resistivity and seismic data: Geophysical Research Letters, **30**, 1-4.

Gallardo, L.A., and Meju, M.A., 2004, Joint two-dimensional DC resistivity and seismic travel time inversion with cross-gradients constraints: Journal of Geophysical Research: Solid Earth, **109** (B3), B03311-B03322

Geyer, R.L., and Martner, S., 1969, SH waves from explosive sources: Geophysics, **34**, 893-905.

Goodman, D., 1994, Ground-penetrating radar simulation in engineering and archaeology: Geophysics, **59**, 224-232.

Hole, J., and Zelt, B., 1995, 3-D finite-difference reflection traveltimes: Geophysical Journal International, **121**, 427-434.

Ivanov, J., Park, C. B., Miller, R.D., and Xia, J., 2000, Mapping Poisson's Ratio of unconsolidated materials from a joint analysis of surface-wave and refraction events: in Proceedings of the Symposium on the Application of Geophysics to Engineering and Environmental Problems (SAGEEP 2000), Arlington, p. 11-17.

Jaiswal, P., Zelt, C.A., and Dasgupta, R., 2008, Near-surface imaging with traveltime and waveform inversion: SEG Technical Program Expanded Abstracts 2008, p. 1865-1869.

King, E.C., and Jarvis, E. P., 2007, Use of shear waves to measure Poisson’s ratio in polar firn: Journal of Environmental & Engineering Geophysics, **12**, 15-21.

Lanz, E., Maurer, H., and Green, A.G., 1998, Refraction tomography over a buried waste disposal site: Geophysics, **63**, 1414-1433.

Lévěque, J.-J., Rivera, L., and Wittlinger, G., 1993, On the use of the checker-board test to assess the resolution of tomographic inversions: Geophysical Journal International, **115**, 313-318.

McBride, J.H., Stephenson, W.J., Williams, R.A., Odum, J.K., Worley, D.M., South, J.V., Brinkerhoff, A.R., Keach, R.W., and Okojie-Ayoro, A.O., 2010, Shallow subsurface structure of the Wasatch fault, Provo segment, Utah, from integrated compressional and shear-wave seismic reflection profiles with implications for fault structure and development: Geological Society of America Bulletin, **122**, 1800-1814.

Rawlinson, N., and Spakman, W., 2016, On the use of sensitivity tests in seismic tomography: Geophysical Journal International, **205**, 1221-1243.

Santamarina, J.C., Rinaldi, V.A., Fratta, D., Klein, K.A., Wang, Y.-H., Cho, G.C., and Cascante, G., 2005, A survey of elastic and electromagnetic properties of near-surface soils: Near-Surface Geophysics, **1**, 71-87.

Scales, J.A., Docherty, P., and Gersztenkorn, A., 1990, Regularization of nonlinear inverse problems-imaging the near-surface weathering layer: Inverse Problems, **6**, 115-131.

Sharma, H.D., Dukes, M.T., and Olsen, D.M., 1990, Field measurements of dynamic moduli and Poisson's ratios of refuse and underlying soils at a landfill site, Geotechnics of waste fills—theory and practice, American Society for Testing and Materials, Philadelphia, p. 57-70.

Sharma, P.V., 1997, Environmental and engineering geophysics, Cambridge University Press, UK, 500p.

Shaw, P.R., and Orcutt, J.A., 1985, Waveform inversion of seismic refraction data and applications to young Pacific crust: Geophysical Journal International, **82**, 375-414.

Tomasi, W., 1987, Electronic Communications Systems: Fundamentals through Advanced, Prentice Hall PTR, 848p.

Williamson, P., 1991, A guide to the limits of resolution imposed by scattering in ray tomography: Geophysics, **56**, 202-207.

Wright, S.G., and Duncan, J. M., 2005, Soil Strength and Slope Stability, John Wiley & Sons, Inc., 500p.

Xia, J., Miller, R.D., and Park, C.B., 1999, Estimation of near-surface shear-wave velocity by inversion of Rayleigh waves: Geophysics, **64**, 691-700.

Xia, J., Miller, R.D., Park, C.B., Hunter, J.A., and Harris, J.B., 2000, Comparing shear-wave velocity profiles from MASW with borehole measurements in unconsolidated sediments, Fraser River Delta, BC, Canada: Journal of Environmental & Engineering Geophysics, **5**, 1-13.

Zelt, C.A., Azaria, A., and Levander, A., 2006, 3D seismic refraction traveltime tomography at a groundwater contamination site: Geophysics, **71**, H67-H78.

Zelt, C.A., and Barton, P.J., 1998, Three-dimensional seismic refraction tomography: A comparison of two methods applied to data from the Faeroe Basin: Journal of Geophysical Research: Solid Earth, **103**(B4), 7187-7210.

Zhang, J., and Toksöz, M., 1998, Nonlinear refraction traveltime tomography: Geophysics, **63**, 1726-1737.

PAPER II

VELOCITY IMAGING WITH FULL WAVEFORM INVERSION IN THE ULTRA-SHALLOW SUBSURFACE, RESULTS FROM P-WAVE DATA – PART 1

3.1 ABSTRACT

Seismic imaging in the ultra-shallow subsurface (within the first few meters) can be challenging when reflections are absent and the data are dominated by ground roll. This paper shows that even when transmission coda is the only phase available for analysis, fine-scale and interpretable P-wave velocity (V_P) and P-wave attenuation (Q_P^{-1}) models of the subsurface can still be prepared using full waveform inversion (FWI). The applicability of FWI is tested through imaging for two ultra-shallow buried targets. The first target is a pair of utility water pipes with known diameters (0.76 m) and burial depth (1.5 m) and the second target is the former location of the pipe(s) which is now a backfilled void and not precisely known. The data for FWI are acquired along a 2D profile using a static array of 24, 40 Hz vertical component phones and buried explosive source. Prior to FWI, as a necessary preconditioning step, ground roll attenuation is attempted in two ways. First, through band pass filtering and muting. Second is a novel wavelet transform-based method known as the redundant lifting scheme (RLS). Results show that a) RLS better suppresses the ground roll coda which in turn aids FWI imaging; and b) V_P and Q_P^{-1} models from FWI could *detect* the two targets but not *differentiate* between them adequately.

3.2 INTRODUCTION

Physical properties of the ultra-shallow subsurface (within the first few meters) soil such as their elastic velocity, density and porosity, is of great interest to many communities such as environmental, engineering and archeological (Bement et al., 2007; Duncan and Wright, 2005; Goodman, 1994; Sharma, 1997). Unfortunately, these properties cannot be measured directly through laboratory testing due to their extremely unconsolidated nature. Instead, indirect measurements can be made through non-intrusive geophysical methods. Seismic methods in particular have potential to play a very significant role in ultra-shallow imaging (Francese et al., 2005; McBride et al., 2010; Pellerin et al., 2009; Zelt et al., 2006). Physical properties affect rigidity and compaction of the soil, which in turn governs the propagation velocity and attenuation of seismic waves (Berryman, 1995). In principle, therefore, through appropriate processing and modeling, physical properties of the ultra-shallow subsurface can be extracted from the seismic coda (Gao et al., 2007; Gao et al., 2006; Romdhane et al., 2011).

Analyzing seismic data for ultra-shallow investigation can be conceptually challenging. Due to their unconsolidated nature, the lithology at these depths may not honor the stress-strain relations which form the basis of conventional acoustic/elastic modeling. Additionally, partially-saturated and/or high-porosity capillary and hyporheic zones tend to attenuate seismic energy in ways that have not yet been fully formulated (Batzle et al., 2005; White, 1975). Interpreting ultra-shallow velocity models can be very different compared to their deeper oil-and-gas counterparts. For example, construction or burial related features such as a steel reinforced concrete pipe or a wooded sarcophagus can have non-standard and much broader range of physical properties as compared to sand- or clay-dominated stratigraphy where physical properties have been well

calibrated to their composition through laboratory tests. Consequently, the interpretation of the ultra-shallow subsurface is driven more by relative changes within the physical property models rather than the absolute value of the physical properties at different model locations (Chen et al., 2013; Jaiswal et al., 2008).

Of all physical properties, seismic velocities are among the most informative. However, in the ultra-shallow, reliably estimating the seismic velocities are nontrivial. Most of the common velocity estimation methods such as the stacking velocity analysis are ray based and rely on collapsing reflection hyperbola (Al-Yahya, 1989). When optical scattering is more prevalent than coherent reflections, which is typical in the ultra-shallow environments, ray-based methods cannot be used. A simple and effective way of generating velocity models in such cases is through analysis of the transmission coda using wave-based tomographic methods such as the full-waveform inversion (FWI) (Smithyman et al., 2009). The ability of FWI in producing high resolution (order of seismic wavelength) physical property images which can be directly interpreted for geological features is now widely accepted (Brenders and Pratt, 2007; Brossier et al., 2009; Kamei et al., 2012; Kumar et al., 2007).

The goal in FWI is to determine an earth model which can replicate the field seismic data, wiggle by wiggle, as closely as possible. Modeling in FWI can be performed both in time and frequency domain, with their own set of pros and cons (Virieux and Operto, 2009). In this paper the modeling is done in frequency domain with visco-acoustic approximation due to computational efficiency and absence of mode-converted energy in the coda of interest. The inverse problem is

solved by minimizing the difference between observed and modeled seismic waveforms, known as data errors, which account for travel-time kinematics as well as amplitude and phase of the seismic waveforms (Gauthier et al., 1986; Tarantola, 1984). Of numerous available methods for minimizing the data errors in the inverse problem, a local descent method, which iteratively refines a starting model by minimizing a function of data errors, is chosen (Pratt, 1999). The starting model required for FWI is prepared by inverting the first arrival times using the regularized Zelt and Barton (1998) method.

The study area in this paper is located in Oklahoma State University's main campus in a sodded field overlying utility pipes. The applicability of combining traveltime and FWI in characterizing the ultra-shallow environment is demonstrated by imaging two ultra-shallow targets, which is the current and former locations of utility water pipes (Figure 1). The current burial depth (1.5m) and diameters (0.76 m) of the utility pipes is known. The former location of the pipe(s) which is now a backfilled void is not precisely known, although a rough estimate is available through vintage construction records. The main challenge in this paper is to accurately locate the position of both targets in presence of low-frequency high-amplitude Rayleigh Waves (referred to as the ground roll hereafter), which dominate the seismic coda. The visco-acoustic nature of the modeling algorithm chosen in this paper requires that the body waves be separated from the ground roll prior to inversion. Two methods of ground roll attenuation are tested. The first is the conventional approach comprising band pass filtering and muting. The second is known as the redundant lifting scheme (RLS); it is a wavelet-transform based image processing method adapted to seismic de-noising (Aghayan et al., 2016).

The data acquired in this paper are typical of the near-surface imaging experiments where due to similar ground roll and body wave velocities the ground roll coda tends to mask the background reflections and transmissions of interest. The field setting in this paper additionally offers an excellent opportunity to test applicability of FWI in near-surface imaging; while imaging at the known pipe location serves as a means of assessing the fidelity of processing and inversion, results elsewhere in the profile may be accordingly interpreted for the unknown target.

3.3 SURVEY AND DATA

Seismic data were acquired along a 23 m long east-west 2D profile at a location where the pipes have a north-south orientation (Figure 1). Data were acquired in a split-spread manner with 24 co-located sources and receivers spaced 1m apart. Sources were buried explosives and receivers were 40 Hz vertical component geophones. No data were recorded at the shot locations. In total, 552 traces were acquired. The field sample interval and trace length were 0.125 ms and 500 ms respectively. The survey was designed such that the present day pipes were located 5-6 m from the east end of the survey leaving ample line length to accommodate the expected backfilled void location. Overall, the unprocessed field data were clean with fairly low random noise. The first arrivals were interpretable up to the farthest source-receiver offsets. No reflections could be identified. As expected in near-surface surveys, low frequency and high amplitude ground roll dominated the coda (Figure 2a). At the preprocessing stage, traces from -2 m to 2 m source-receiver offset were muted due to waveform clipping of the first arrivals.

3.4 METHODS

3.4.1 REDUNDANT LIFTING SCHEME (RLS)

Sweldens (1996) developed a wavelet transform based method for image processing to sharpen the object boundaries and suppress random noise and referred to it as the Lifting Scheme (LS). Claypoole et al. (1998) corrected aliasing which was inherent in LS and referred to the modified method as Redundant Lifting Scheme (RLS). Aghayan et.al. (2016), demonstrated how RLS can be used with seismic data for removal of coherent and incoherent noise. In this application, RLS is used for isolating the high-amplitude low-frequency ground roll. A brief introduction to these methods is provided below and the reader is guided to the original references for details.

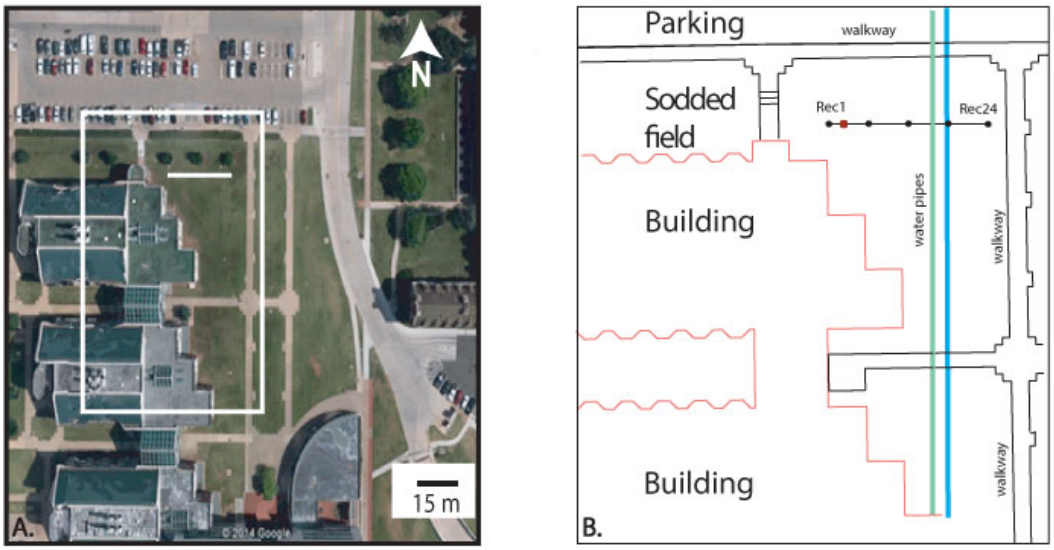

Figure 1: Base map. A) Google Earth image of Oklahoma State University's Main Campus. The study area is outlined with a white box. B) Sketch of the study area showing the location of the

seismic line and the utility water pipes and the buildings. Data for the third source (red dot) is shown in Figure 2.

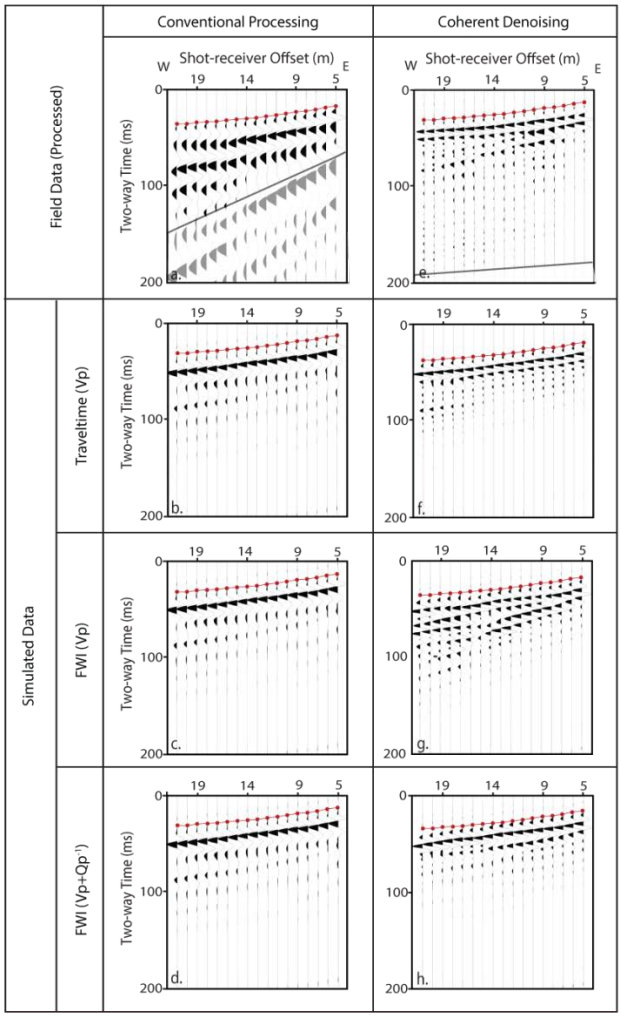

Figure 2: Representative data. a) Dataset from conventional processing. (b) – (d) simulated data from traveltime, FWI V_P, and FWI $V_P + Q_P^{-1}$ models. Models in (b) - (d) are obtained from inversion of conventional processing. e) Dataset from coherent denoising (RLS processing). (f) – (h) are same as (b) – (d) except that the models are obtained from inversion of coherent denoise data.

The LS has a forward (Figure 3a) and an inverse (Figure 3b) part. The forward part has three steps:

i. Split: The time series, $x[n]$, is divided into two subsets: $x_e[n] = x[2n]$, representing the even indexed part, and $x_o[n] = x[2n+1]$, representing the odd indexed part of the signal.

ii. Predict: A wavelet coefficient, $d[n]$ is generated which is the error in predicting $x_o[n]$ from $x_e[n]$ using the prediction operator $\wp$:

$$d[n] = x_o[n] - \wp(x_e[n]) \quad (1)$$

iii. Update: The wavelets $x_e[n]$ and $d[n]$ are combined to obtain a scaling coefficient series, $c[n]$ which is an approximation to the original time series $x[n]$. This is achieved by applying an update operator $\mathfrak{U}$ to the wavelet coefficient and adding it to $x_e[n]$:

$$c[n] = x_e[n] + \mathfrak{U}(d[n]) \quad (2)$$

Recursively splitting $x[n]$ creates a complete set of discrete wavelet transform scaling $c_j[n]$ and wavelet co-efficients $d_j[n]$. The lifting steps are inverted comfortably even if $\wp$ and $\mathfrak{U}$ are non-linear or non-invertible. The inverse part (Figure 3b) is relatively straightforward. Equations 1 and 2 merely need to be rearranged to obtain the original, odd and even, series.

$$x_e[n] = c[n] - \mathfrak{U}(d[n]) \quad (3)$$

$$x_o[n] = d[n] + \wp(x_e[n]) \quad (4)$$

A major limitation of the LS is that it does not preserve the entire length of signal at each level of recursive splitting, which causes aliasing. To overcome this, Claypoole et al. (1998) proposed a modification at the prediction stage, which also translates into a modification at the update stage.

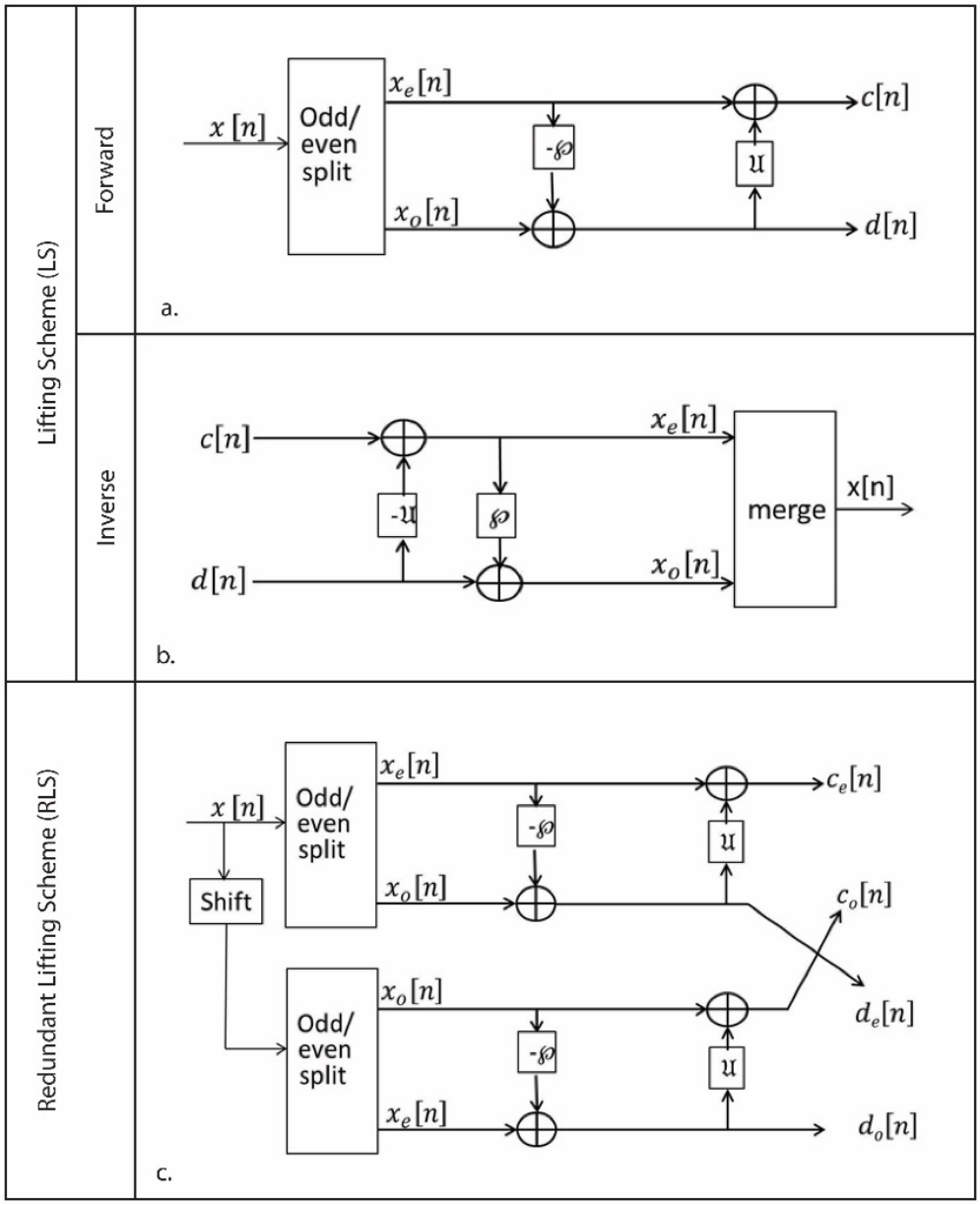

Figure 3: Lifting Scheme (LS) and RLS flow charts. a) Forward LS. b) Inverse LS. c) RLS.

The new, RLS method (Figure 3c), can be summarized as follows:

i. Predict: Instead of splitting the signal in disjoint sets of odd and even indexed sample, each sample is predicted by its adjacent sample using a predictor operator $\wp$:

$$d[j] = x_n[j] - \wp(x_n[j-1]) \quad (5)$$

Where, $x_n$is the time series and *j* is the sample index.

ii. Update: Using the prediction error, the update operator $\mathfrak{U}$ preserves the characteristics of the original signal as:

$$c[j] = x_n[j] + \mathfrak{U}(d[j]) \quad (6)$$

After decomposing the signal into $d[j]$ and $c[j]$, a threshold denoising can be applied (Aghayan and Jaiswal, 2014 *in review*). In this step, coefficients less than a pre-defined magnitude are set to zero. The threshold, (τ), is based on the standard deviation of noise (Donoho and Johnstone, 1994): $\tau = \sigma\sqrt{2\ln(l)}$ (7)

In Equation 7, $\sigma = \frac{1}{0.6745}(median(d(n)))$, is standard deviation of noise. Finally soft thresholding based noise elimination is performed as:

$$X_\tau(n) = f(x) = \begin{cases} X(n) - \tau, \ for\ X(n) \geq \tau \\ X(n) + \tau\ for\ X(n) \leq \tau \\ X(n) = 0\ for\ |X(n)| < \tau \end{cases} \quad (8)$$

In Equation 8, X(n) is unfiltered d[j] or c[j] and $X_\tau(n)$ is filtered $d[j]$ or $c[j]$. After applying the thresholding the original time series can be reconstructed using the following approach:

$$x^u{}_n[j] = c[j] - \mathfrak{U}(d[j]) \quad (9)$$

$$x^p{}_n[j] = d[j] + \wp(d[j]) \quad (10)$$

$$x[j] = \frac{1}{2}(x^u{}_n[j] + x^p{}_n[j]) \quad (11)$$

Before applying the RLS method to seismic data in this paper a synthetic test is performed to ensure this method's fidelity (Figure 4). Synthetic shot data with both ground roll and body

waves were simulated using similar acquisition parameters and frequency bandwidth as the unprocessed field data. For modeling the ground roll the linear elastodynamic equation (Aki and Richards, 2002) is solved using the Spectral Element Method (Ampuero, 2008). Ground roll modeling through this algorithm requires setting of Courant-Freidrichs-Levy (CFL) number (Strikwerda, 2004):

$$CFL = \frac{|u|\Delta t}{\Delta x} \leq 1 \qquad (12)$$

In equation 12, $|u|$ is the minimum V_P in the model, assumed as 200 m/s corresponding to the near-surface sediments, and Δt and Δx are the space and time finite-difference steps respectively. Higher CFL number increases model stability. However, it also increases the required number of grid points per wavelength which in turn increases the space-time computation complexity. Larger time steps can reduce computation time but at the expense of numerical dispersion. In the end, a tradeoff is made between numerical dispersion and computation time.

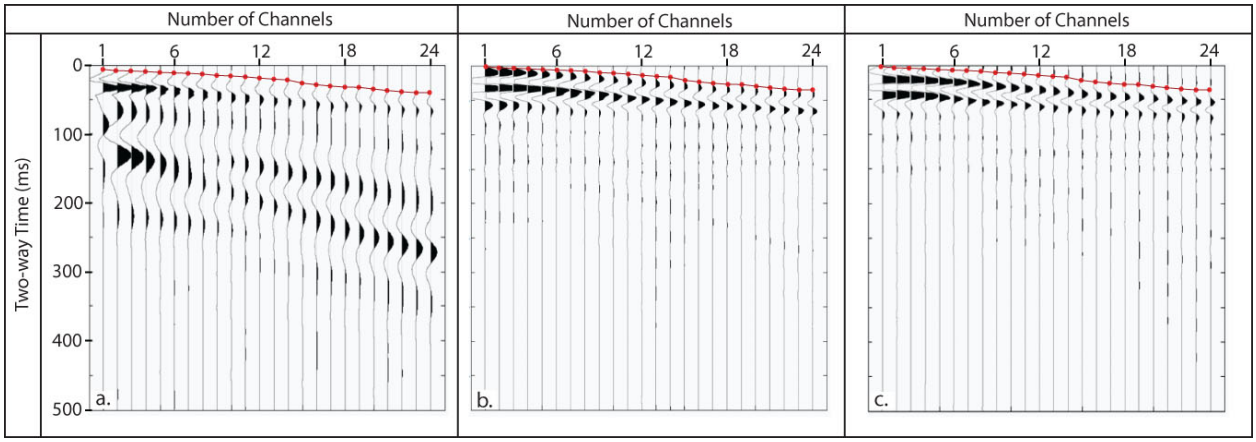

Figure 4: Synthetic RLS test. a) Shot gather with ground roll and transmission coda. b) Ground roll removal by RLS based processing. c) Processed data after phase rotation such that the first breaks are positioned at the beginning of a trough.

Generally the ground rolls have a lower frequency bandwidth than the reflections or transmissions. The synthetic shot data were therefore made by creating two separate wavefields with different frequency bandwidths and superimposing them. The first was a wavefield with broader frequency wavefield which contained only reflections and transmission and the second was a lower-frequency wavefield which only contained the ground roll. The data were superimposed such the ground roll were substantially stronger than the reflections or transmissions (Figure 4a), which is similar to unprocessed field data. Trace-by-trace application of RLS using Equations 5 – 11 effectively attenuated the ground roll but resulted in a net phase shift (~17^0; Figure 4b). This was due to the zero-phase coefficient wavelet used in coherent denoising. The synthetic test suggested that although RLS is effective in ground roll attenuation, the data have to be phase-rotated prior to FWI.

3.4.2 TRAVELTIME & FULL WAVEFORM INVERSION

Although the traveltime inversion in this paper is only used to create a starting model for FWI, the two inversion methods have many similarities. In both methods an initial model is updated iteratively to achieve a satisfactory misfit between the real and predicted data. When the inversion dataset comprises traveltimes only, the outcome is a large-scale (order of Fresnel zone) velocity image of the subsurface. When the inversion dataset is "whole coda," the outcome is a finer-scale (order of wavelength) velocity image. The forward modeling in both methods is implemented on a finite-difference grid. The traveltime method solves the eikonal equation (Equation 13) using a scheme modified to handle large velocity variations (Hole and Zelt, 1995).

$$\left|\nabla t\right|^2 = \frac{1}{c^2} \tag{13}$$

In Equation 13, c is the slowness, Δt is the delay time, and $c\nabla t$ is a unit vector in the direction of the ray. The waveform method solves the visco-acoustic wave equation (Equation 14) using the mixed-grid approach (Jo et al., 1996) which accounts for backscattering and wide-angle effects.

$$d_{pre}(\omega)=S^{-1}(\omega)f(\omega) \quad (14)$$

In equation 14, $\boldsymbol{d}$ is the complex-valued wavefield from model $\boldsymbol{m}$, $\boldsymbol{S}$ is a complex-valued impedance matrix that contains information about the physical properties of $\boldsymbol{m}$, and $\boldsymbol{f}$ is the source-term vector.

The inverse problem in both methods satisfies convergence criteria, but with different formulation of the decent method. Both methods define an objective function and minimize it. In traveltime inversion the objective function, $E(m)^{TT}$ is the L_2 norm of a combination of data errors and model roughness (Equation 15), while in the waveform method the objective function $E(m)^{WV}$ is the L_2 norm of data errors only (Equation 16).

$$E(m)^{TT} = \Delta d^T C_d^{-1} \Delta d + \lambda [m^T C_h^{-1} m + s_z m^T C_v^{-1} m] \quad (15)$$

$$E(m)^{WV} = \Delta d^T \Delta d \quad (16)$$

In equations 15 and 16, $\Delta d = d_{pre} - d_{obs}$ are data errors, and d_{pre} and d_{obs} are predicted and observed data (arrival times or the entire wavefield). In equation 15, C_d is the data covariance matrix, C_h and C_v are model space covariance matrices that measure horizontal and vertical roughness respectively, λ is the trade-off parameter, and s_z determines the relative importance of maintaining vertical versus horizontal model smoothness.

In general, if m^k is the model in the k^{th} iteration, $\boldsymbol{\delta m}$ is defined as the model perturbation such that $m^{k+1} = m^k + \delta m$. For the traveltime inversion $\boldsymbol{\delta m}$, is computed using strategy (Shaw and Orcutt, 1985).

The regularization in traveltime inversion, implemented by scaling with the inverses of the data and model space covariance matrices, attempts to obtain the smoothest model appropriate for the data errors (Scales et al., 1990) (Equation 17).

$$\begin{bmatrix} C_d^{-\frac{1}{2}} L \\ \lambda C_h \\ s_z \lambda C_v \end{bmatrix} \delta m = \begin{bmatrix} C_d^{-\frac{1}{2}} L \\ -\lambda C_h m_0 \\ -s_z \lambda C_v m_0 \end{bmatrix} \tag{17}$$

In equation 17, L is the partial derivative matrix of the data errors with respect to the model parameters. See appendix for derivation of Equation 17 from Equation 15.

In waveform inversion, $\boldsymbol{\delta m}$ is expressed as:

$$\delta m = -\alpha^k \nabla . E^k(m) \tag{18}$$

In equation 18, $\nabla E(m)$ is the gradient direction, and α is a scalar which replaces the Hessian (Pratt, 1999); in practice it is the step length chosen using a line-search method. The key in the (Pratt, 1999) method is to express the gradient direction as:

$$\nabla E(\mathbf{m}) = \frac{\partial E}{\partial \mathbf{m}} = Real\{\mathbf{F}^t[\mathbf{S}^{-1}]^t \delta \mathbf{d}^*\} \tag{19}$$

In equation 19, $\boldsymbol{F}$ is known as a virtual source, which can be understood as the interaction of the $\boldsymbol{d_{obs}}$ with the perturbations in $\boldsymbol{m}$. Individual elements of the virtual source are defined as

$\mathbf{f}^{i} = -\frac{\partial \mathbf{S}}{\partial \mathbf{m}_{i}}\mathbf{d}_{\mathbf{obs}}$, where $\mathbf{f^i}$ and $\mathbf{m_i}$ are the *i*-th virtual source and model parameter respectively. This is the mathematical expression of the back-propagated residual wavefield $[\boldsymbol{S}^{-1}]\delta\boldsymbol{d}$ being correlated with the forward propagated wavefield $\boldsymbol{F}$. The computational complexity in waveform inversion rests predominantly on computing $\boldsymbol{S}^{-1}$. For multiple source problems, $\boldsymbol{S}^{-1}$ is best solved using LU decomposition (Press et al., 1992) and ordering schemes such as nested dissection, which take advantage of the sparse nature of $\boldsymbol{S}$ (George and Liu, 1981; Marfurt, 1984).

The biggest difference in traveltime and waveform inversion is in the stopping criterion. Traveltime inversion is halted based on the user-defined range of data uncertainty of the observed data. In waveform inversion stopping criteria are qualitative. Usually the iterative updates to the model are halted for a given frequency (or group of frequencies) when the objective function ceases to reduce any further. A visual assessment of the updated model for its overall geologic sensibility and comparison of the predicted wavefield for similarity to the real wavefield can additionally serve as a justification for halting. Unlike traveltime inversion, FWI also requires a source function. In the Pratt (1999) method, the source function is estimated with the help of the current model. Thus, waveform inversion begins not only with a starting model but also a starting source signature. For a given bandwidth, the velocity model is first updated using a priori source signature and then the source signature is updated using the updated velocity model. In the end, as higher frequencies are incorporated in the source signature the resolution of the recovered model is enhanced.

3.5 APPLICATION AND RESULTS

3.5.1 TRAVELTIME INVERSION

In all the shot records first arrival times could be easily identified to the farthest source-receiver offsets. In total, 552 arrival times were inverted. An uncertainty of 1ms was assigned based on the dominant frequency and signal-to-noise ratio. The starting model for traveltime inversion was essentially 1-D; 200 m/s at the topography linearly increases to 1800 m/s at 20 m depth (base of the starting model). The traveltime inversion converged in 15 iterations and yielded a smooth model (Figure 5a). Following the Jaiswal et al. (2009) strategy, checkerboard resolution tests were used to determine that the traveltime model has a resolution corresponding to at least 35 Hz frequency, which is the lowest frequency available for use in the FWI.

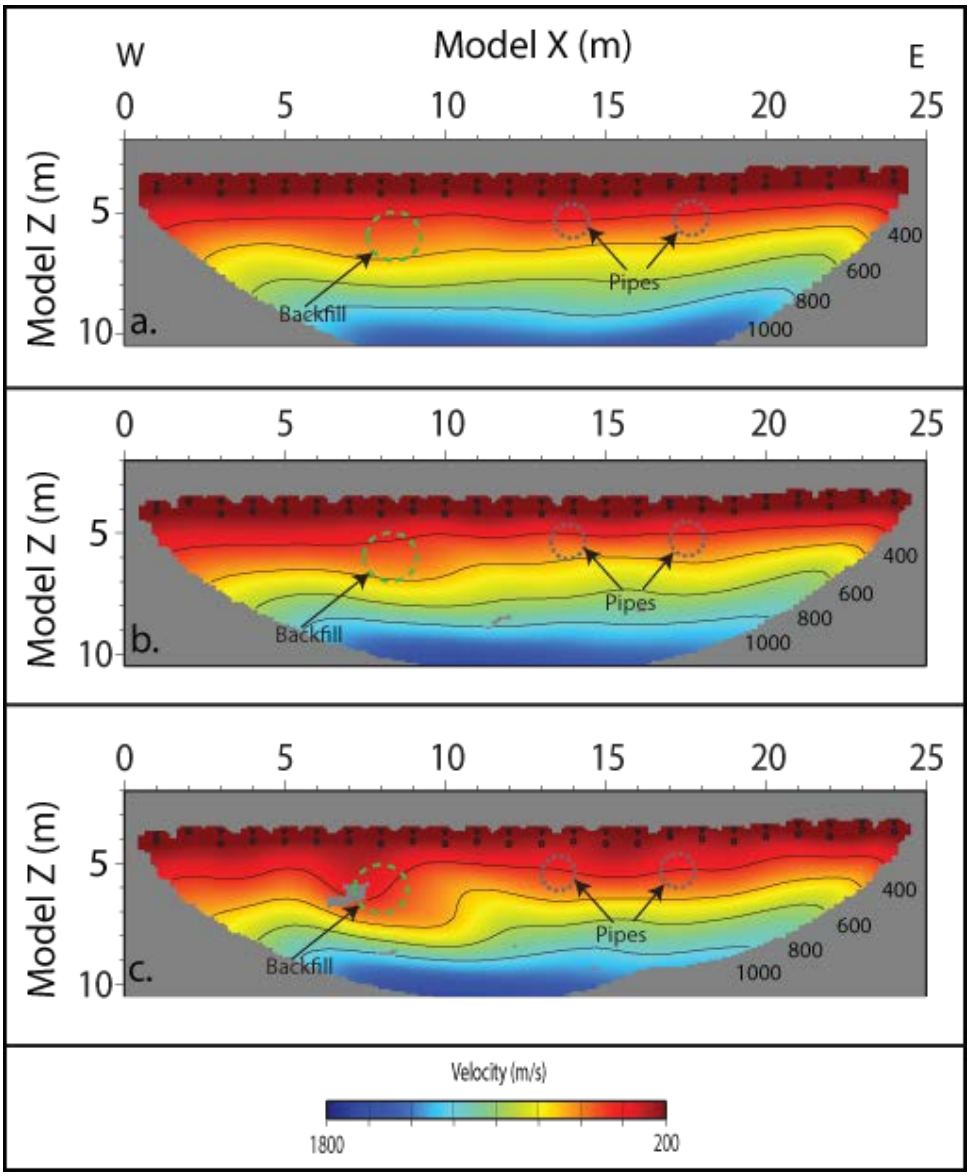

Figure 5: P-wave velocity (V_P) models from a) Travetime inversion. b) FWI of dataset with conventional processing. c) FWI of dataset with coherent denoising. Note the velocity structure in (c) at the location of expected anomaly. In (a) – (c) triangles and solids dots are receiver and source locations. The current pipe locations are shown in black dashed circles. The backfill location interpreted based on the perturbations (Figure 5), is outlined in a green dashed circle.

3.5.2 DATA PREPARATION FOR FWI

Data preparation of FWI involved suppression of phases such as ground roll and mode converted energy that is beyond the physics of visco-acoustic modeling. Effects of other non-physical factor such as source directivity were minimized by a general amplitude scaling and shot-to-shot amplitude balancing. Mode-converted energy was not assumed to be present, although this assumption could be a potential source of error. Ground roll have a strong presence in all shots (Figure 2a). Two methods were adopted to attenuate ground roll which resulted in creation of two datasets for FWI.

The first method is rather conventional which includes 10-20-200-400 Hz band pass filter, top mute above the first arrivals, an interpretive bottom mute so as to completely remove the ground roll, and resampling at 1ms and trace truncation at 200 ms. Data processed in this manner is hereafter referred to as the conventionally processed data (figure 2a). The second method was application of RLS followed by a phase rotation of 20^0 so as to place the first arrivals at the onset of a trough as observed in the unprocessed field data, 1 ms resampling, trace truncation at 200 ms, top muting, 0-10-100-150 ms cosine taper starting at the first arrivals and a bottom mute 150 ms below the first arrivals. Data processed in this manner is hereafter referred to as the Coherent deoised data (Figure 2d). In both datasets a general post-processing scanning and editing was done to remove noisy traces leaving 432 traces to be used for FWI.

3.5.3 SOURCE AND MODEL UPDATE

Using the starting model (Figure 5a) FWI begun by estimating a source signature for conventionally processed data (Figure 6a) and coherent denoised data (Figure 6d). Using this source, a group of three frequencies – 35, 40 and 45 Hz was simultaneously inverted. This was the lowest frequency group which yielded geologically reasonable updates (Figure 7a and d for Datasets 1 and 2 respectively). Following this, the inversion frequencies were increased in a bootstrap manner. Inverting every frequency did not result in model improvements. Past the lowest frequency group, most reasonable model updates were obtained by inverting only two other groups - 75, 80, 85 Hz (Figures 7b and e) and 155, 160, 165 Hz (Figures 7c and f). The updated model from each step was used as the starting model for the next step. Before updating the model in each step, the source signature was recalculated using the updated model from the previous step. At each inversion step, iterations were continued until the reduction in the objective function's value was less than 1%.

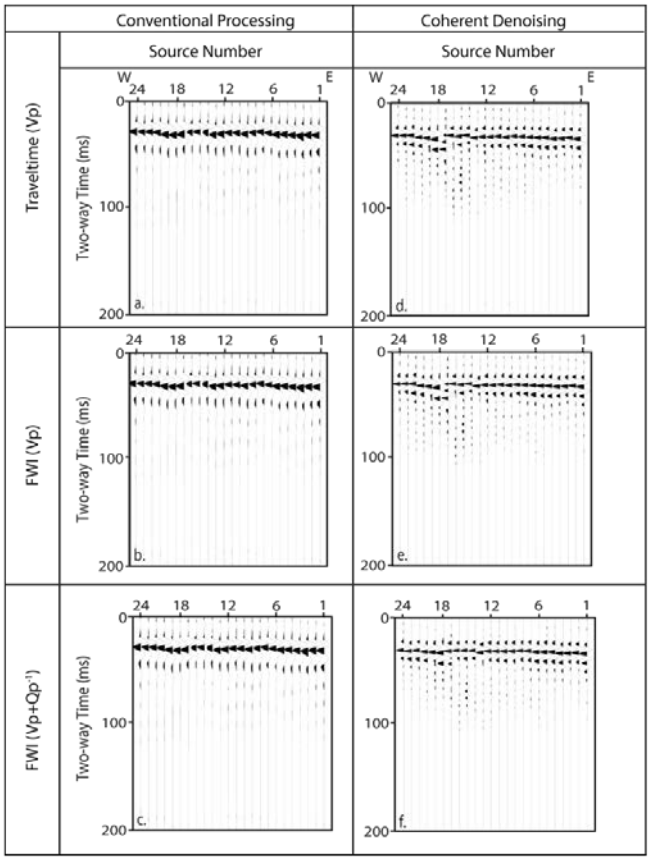

Figure 6: Inverted Sources. a) Traveltime V_P model, b) FWI V_P model and c) FWI $V_P + Q_P^{-1}$ models. Models in (a) – (c) are obtained by inverting conventionally processed data. (d) – (f) are same as (a) – (c) except that models are obtained by inverting coherent denoise dataset. Sources successively become more consistent as velocity and attenuation models are created.

For both datasets, the inversion of lowest frequency group yielded a smooth velocity updates where the perturbations did not show any clear coincidence with the pipe location. Incorporation of higher frequencies in each step yielded a higher wave number solution of the velocity model with perturbations becoming localized around the known pipe locations. At inversion frequencies higher than 160 Hz, it became increasingly more difficult to distinguish between what are

genuine anomalies versus model artifacts. A judgment call was made to designate the model from 165 Hz inversion as the final model.

The final model from both datasets shows a V_P reduction of ~20% at two zones, one at the current pipe location and the other, most likely, at the location of the backfilled void (fig..). The V_P perturbations from FWI of coherent denoise dataset appear to be better focused. The source character also changed in successive iterations of FWI. The source from 30 – 40Hz frequency has a rapidly shot-to-shot varying strength (Figure 6a and d). Sources became somewhat more consistent as higher frequencies were inverted (Figure 6b-c and e-f). Unlike a marine survey, sources in a land survey are not expected to be identical. However, some improvement in source consistency is expected as a result of the inverted model approaching the true earth model.

The final FWI models (Figure 7c and f) were used as a starting model for attenuation inversion. This is a nominal procedure which assumes that the first order amplitude variations in the data are due to optical focusing while the higher order variations are attenuation driven. Initially no background attenuation was assumed. The frequency groups used for attenuation inversion were not the same for both datasets as they were for the velocity inversion. In the first dataset 25-30-35 Hz, 40-45-50 Hz, and 70-75-80 Hz frequency groups were sequentially inverted. In the second dataset 25-30-35Hz, 40-45-50Hz, and 55-60-65Hz were sequentially inverted. Like the velocities for both datasets, the attenuation inversion was halted based on geological sensibility of the updates and convergence of the objective functions (Figure 8). Final attenuation model

from coherent denoise data (Figure 8f), appears to be the most reasonable representation of the current and former pipe locations.

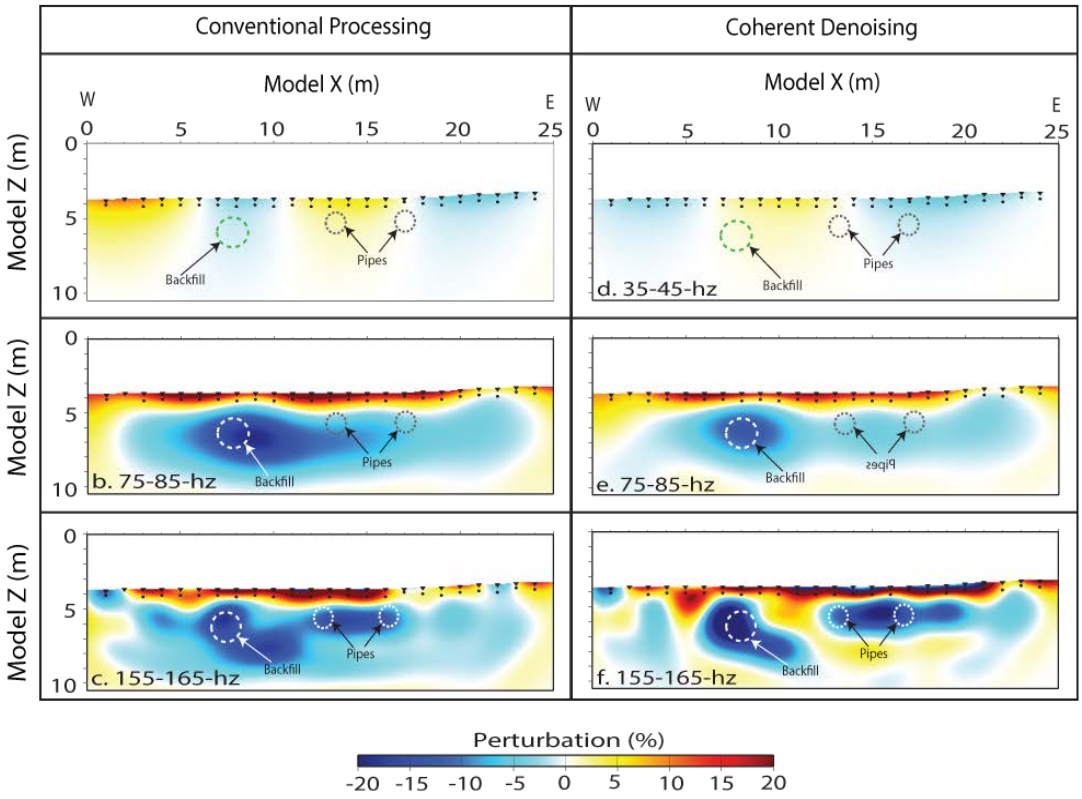

Figure 7: FWI V_P perturbations. (a) – (c) are from inversion of 35-40-45 Hz, 75-80-85 Hz, and 155-160-165 Hz respectively from conventionally processed data. (d) – (f) and same as (a) – (c) except that the inversion corresponds to coherent denoise data. In (a) – (f) triangles and solid dots are receiver and source locations, current pipe locations are shown by the two dashed circles in the eastern side of the model and the backfill is interpreted by the white/green dashed circles in western side of the model.

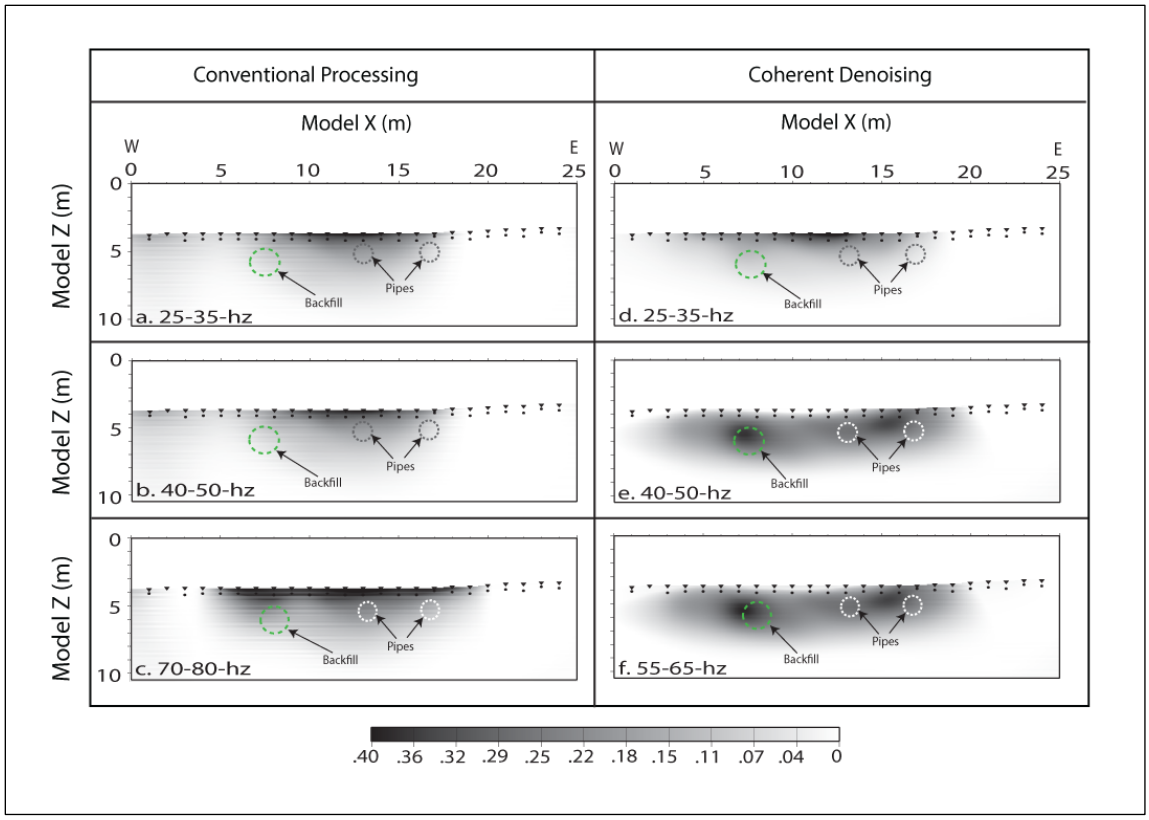

Figure 8: FWI Q_P^{-1} models. (a) – (c) are from inversion of 25-30-35 Hz, 40-45-50 Hz, and 70-75-80 Hz respectively from conventionally processed data. (d) – (f) are same as (a) – (c) except that the inversion corresponds to coherent denoise data from 25-30-35Hz, 40-45-50Hz, and 55-60-65Hz respectively. In (a) – (f) current pipe locations are shown by gray/white dashed circles. Backfill, based on Figure 7, is outlined in green dashed ellipse.

3.5.4. MODEL ASSESSMENT

The FWI V_P perturbations were assessed using single anomaly resolution tests (Figure 9). The final FWI V_P for both datasets were perturbed by -20% at the interpreted anomaly locations. The dimensions and the magnitude of the perturbation were in line with the real anomalies. Three

synthetic datasets were simulated using a) the ideal source and final inverted sources from b) conventionally processed data (Figure 6c); and c) coherent denoised data (Figure 6f). The synthetic data were inverted in the same manner as the processed field data. Results suggest that V_P perturbations in Figure 7 were realistic.

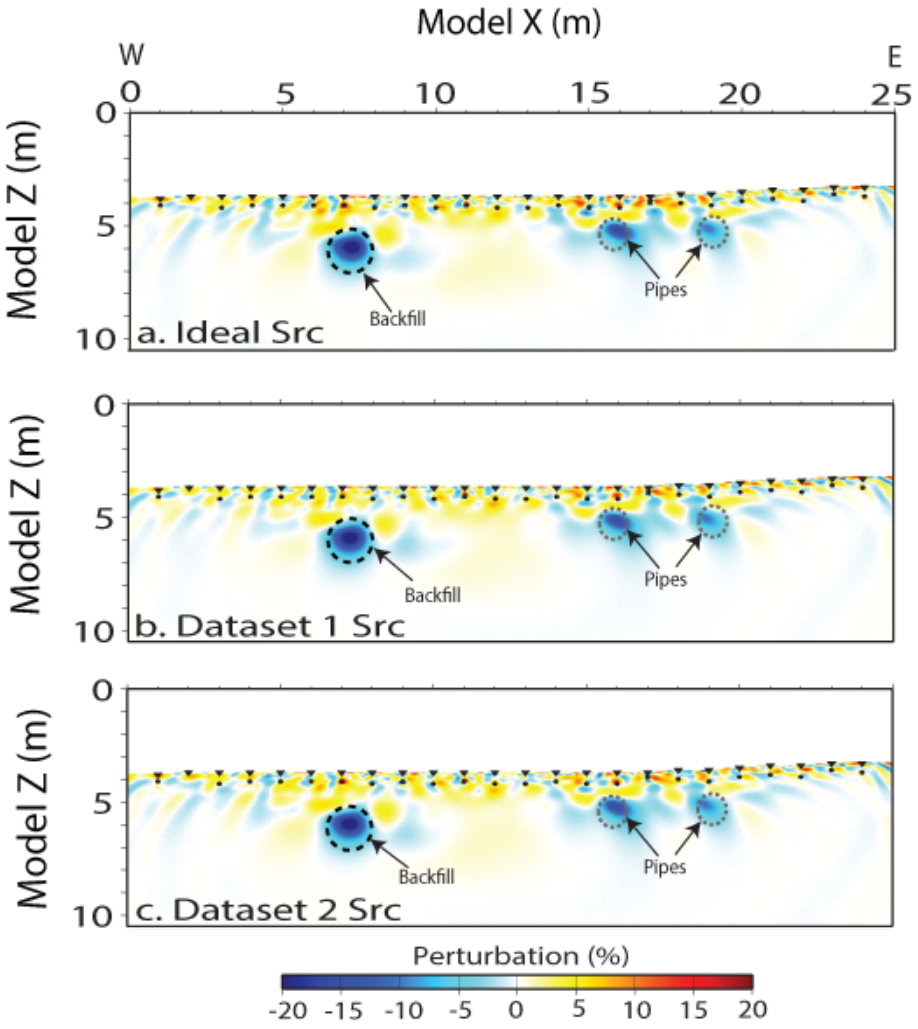

Figure 9: Single anomaly resolution test. a) Inversion of data simulated using a) Ideal source, b) final source for conventionally processed data (Figure 6c), and c) final source for coherent denoised data (Figure 6f). In (a) – (c) black and gray dashed circles represent the backfill and pipes respectively.

The final models were further assessed by comparing the first arrival and root mean square (RMS) amplitudes of both datasets with their counterparts simulated from the traveltime and FWI models with respective sources (Figure 10). Figures 10a, b and c show the first arrival errors respectively corresponding to traveltime, FWI V_P and FWI $V_P+Q_P^{-1}$ models for conventionally processed data. Figures 10d – f are same as a – c, computed for coherent denoise data. Figures 10g, h and i are RMS errors respectively corresponding to traveltime, FWI V_P and FWI $V_P+Q_P^{-1}$ models for conventionally processed data. Figures 10j – l are same as g – i, computed for coherent denoise data.

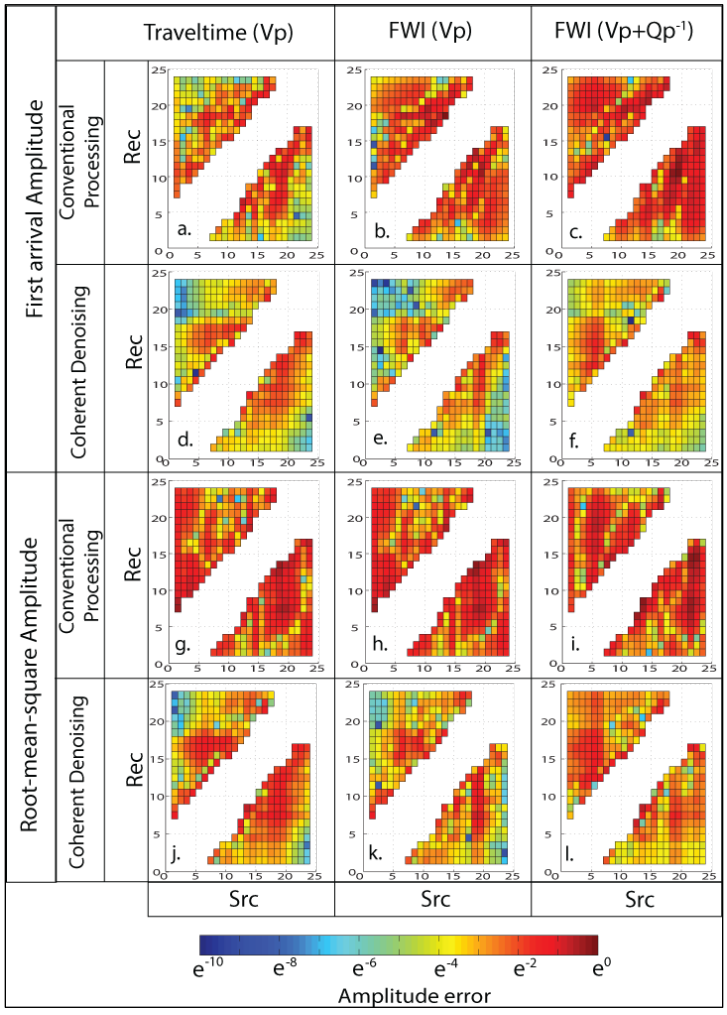

Figure 10: Amplitude comparison. Difference in first arrival amplitude between conventionally processed data and simulated data from a) traveltime V_P and the corresponding inverted source, b) FWI V_P and the corresponding inverted source and c) FWI V_P + Q_P^{-1} and the corresponding inverted source. (d) – (f) are same as (a) – (c) except that results are for coherent denoise data. (g) – (l) same as (a) – (f) except that the results are for whole trace root-mean-square amplitude.

In Figure 10, warmer colors represent higher error. As evident, data simulated from FWI models do not appear to be getting closer to their respective inputs in all cases. In fact, the first arrival amplitude error in conventionally processed data increases through the FWI process. The first arrival amplitudes error in coherent denoise data improve from traveltime to FWI V_P model (Figure 10d and e) but deteriorate when the attenuation model is included in data simulation (Figure 10f). The RMS amplitude errors for conventionally processed data also show a rather marginal improvement, mostly in the mid-offsets, through the FWI process. The RMS amplitude errors for coherent denoise data show a reasonable decline through the FWI process, both in the near- and the mid-offsets; error reduction from traveltime to FWI V_p modeling (Figures 10j – k) are more than reduction from FWI V_P to FWI Q_P^{-1} modeling. Although error reduction is very modest, in a relative sense V_P and Q_P^{-1} perturbations from FWI of coherent denoise data can be considered reliable with V_P perturbations more reliable than the Q_P^{-1} perturbations in general.

3.5.5 MODEL INTERPRETATION

The spatial location of the utility pipes can be better identified in the V_P perturbation model from coherent denoise data (Figures 7f). Besides perturbations at the known location of the utility

pipes, in both images distinct velocity perturbation is also seen at model distance 7 m and depth 1.5 m. The definition of this anomaly is much better in inversion results of the coherent denoise data compared to conventionally processed data. This location is most likely the location of the backfilled void. As suggested in Figure 7 f, the area encompassed by backfilled void is larger than the area encompassed by a single utility pipe, which could be the result of excavation around the pipe location. It also seems like originally only one utility pipe was laid.

Much like its V_P counterparts, the attenuation models from the coherent denoise data (Figure 8f) also show two distinct anomalies. The first coincides with the location of one of the utility pipes and the second with the backfilled void. On the other hand, the attenuation model from conventionally processed data (Figure 8c) does not have any indications of the pipes or the backfilling unlike its V_P counterpart. In Figure 8c, a general increase in attenuation closer to the surface can be seen, which is intuitively correct but not reflective of the buried targets. On a related note, the magnitude of the attenuation from both datasets remains fairly low. However, much like their V_P counterparts the absolute magnitude of attenuation is rather meaningless. It is only in a relative sense that the attenuation changes indicate the location of the buried targets.

3.6 DISCUSSION

Velocity imaging of the near surface is rather challenging. Models from stacking or even migration velocity analysis may be too general for near-surface interpretation purposes. Rapidly varying soil compaction, seasonal changes in saturation and anthropogenic artefacts, such as objects from past construction or burial increases the complexities of velocity structure. FWI

offers a reliable way of imaging fine-scale velocity and attenuation subsurface variations. A notable benefit of FWI is that it can yield the velocity image using transmission coda which is generally discarded in conventional processing. Although FWI converged for both datasets in this case study, the resulting models would be difficult to reply upon if fidelity of the inverted models were solely assessed through amplitude comparison (such as in Figure 10). However, in this particular case, *a-priory* knowledge of one of the targets provided confidence in inversion results. In retrospect, burying an appropriately sized object at a known location and depth might be a useful strategy when FWI is being used for ultra-shallow imaging.

A multitude of reasons could have been responsible for little to no improvement in amplitude prediction. First, the sediments under investigation may be non-hookean in nature with a varying degree of deviation from the elastic theory, as one gets closer to the surface. Second, even if no mode conversion is assumed, poro-elasticity rather than a viso-acoustic approximation could have better described the propagation media. Third, coherent noise with unknown and unexpected pattern besides the ground roll (Robertsson et al., 1996), such as those related to water flow in the pipe, could have had a remnant presence in both datasets. It appears that attenuation of the ground roll coda made the biggest impact in the quality of inversion results. Here, a wavelet-transform based method was used but several other techniques exist in the literature, such as using the curvelet domain (Yarham and Herrmann, 2008), polarization filter (Shieh and Herrmann, 1990), seismic interferometry (Halliday et al., 2007) or the modified Sacchi (2002) method based on Karhunen-Loève transform (Londoño et al., 2005). Unfortunately, most of these methods could not be applied to the datasets in this paper probably due to the extremely short recording time and absence of reflections. On a related note,

comparing and contrasting all possible ground roll removal methods is somewhat out of this paper's scope.

In waveform inversion, the starting model must be close to the true model to satisfy the born approximation in seeking a solution of the wave equation. This makes waveform inversion only valid for weak scattering (Aki and Richards, 1980). Based on the magnitude of the perturbation in the final model, ~20%, it can be argued that the scatter in our case study is not weak. The validity of the waveform inversion needs to be understood in this context of its multi-scale approach. Imaging through FWI requires that the entire set of wavenumbers that constitute a given velocity anomaly be reconstructed. The reconstruction proceeds from the larger to the smaller wavenumbers by iteratively inverting selective groups of frequencies in increasing order. The updated model from an individual group is used as a starting model for the next group. For an individual group, the updates were weak, i.e., the final model is close to the starting model. Thus, FWI results in this case study were theoretically sound. It is just that the model perturbation (anomaly) gains strength cumulatively over multiple frequency groups.

The starting model plays a crucial role in the success of waveform inversion. The starting model in this study was generated from traveltime inversion at a length scale corresponding to the wavenumbers lower than those corresponding to the minimum frequency used in FWI. Unfortunately, unless the velocity field is constant, there is no straightforward way of estimating the wavenumber content. Many authors have used checkerboard tests, which are accurate to the first order of approximation (Jaiswal et al., 2008). Besides having appropriate wavenumber

content, the starting model also needs to predict arrival times within quarter –wavelength of the unprocessed field data to prevent cycle skipping (Sirgue and Pratt, 2004). In this case study resolution test and wavefield simulations were used to ensure that inversion of first arrival traveltime yielded reasonable model for waveform inversion.

Although initially heuristic in nature, we realized that the maximum updates were obtained from inversion of three frequency groups only. The grouping was heuristically done through trial and error. Grouping in sets of 3 at 5 Hz interval led to the most minimization of the objective function while maintaining a good S/N in the inverted model. The inferences were similar for datasets from both processing approaches. The expected anomalies appeared in both V_P models; although the models from inversion of coherent denoise data were more meaningful. In the end, the results were presented for identical frequencies for both datasets. The choice of these frequencies however was not intended to bias the results towards one dataset. It was a natural outcome of model updates and objective function reduction.

Attenuation is the least understood aspect of frequency domain FWI. In this case study attenuation is implemented by considering acoustic velocities as a complex entity. Many other mechanistic aspects of lithology such as differential compaction and partial saturation that is known to effect attenuation could not be incorporated into modeling. Despite its limitation complex velocity assumption provides reliable results, at least for coherent denoise dataset. The biggest shortcoming of this case study is the inability of the P-wave data in differentiating between the two buried targets. The velocity perturbation at both target location were almost

identical. The attenuation updates were similar. P-waves only image bulk properties (combined effect of solid and fluids). Although the acquisition was performed during the dry period, water from the lawn sprinklers in the backfilled zone could have made it appear acoustically similar to the zone with utility pipes where water is actively being transported. Inversion of shear waves, which are more sensitive to matrix properties than the pore-fluids, may provide more insights.

3.7 CONCLUSION

This paper presents a successful case study of detecting buried targets in the ultra-shallow subsurface using traveltime and waveform inversion. The first target, a set of utility pipes, was of known dimension and burial depth. The second target, the former pipe location which is now backfilled, was unknown prior to the imaging experiment. FWI successfully detected both targets as zones of velocity decrease with respect to a simple starting model prepared from inversion of first arrival times. Besides the fidelity of the starting model, FWI's success depended on attenuation of ground roll. Here, a novel wavelet transformation based method proved between in ground roll attenuation than the conventional approach of band pass filtering followed by muting. This study suggests that with careful acquisition, data-preconditioning and modeling traveltime and full waveform inversion can be a promising tool in ultra-shallow seismic imaging.

3.8 ACKNOWLEDGMENTS

The seismic data in this study were acquired with the help of Salman Abbasi, Pouyan Ebrahimi and Brooke Briand. The physical plant at Oklahoma State University provided the blueprint and

scoped the problem. The Boone Pickens School of Geology and Geophysical Society of Oklahoma State University chapter partially funded the survey.

3.9 REFERENCES

Aghayan, A., and Jaiswal, P., Siahkoohi, H.R., 2016, Seismic denoising using Redundant Lifting Scheme: Geophysics, v.81, no. 3, p. v249-v260.

Aki, K., and Richards, P., 1980, Quantitative Seismology: Theory and Methods: Volume I: WH Freeman & Co.

Aki, K., and Richards, P. G., 2002, Quantitative seismology.

Al-Yahya, K., 1989, Velocity analysis by iterative profile migration: Geophysics, v. 54, no. 6, p. 718-729.

Ampuero, J., 2008, SEM2DPACK: A spectral element method tool for 2D wave propagation and earthquake source dynamics–User's Guide Version 2.3. 4.

Batzle, M., Hofmann, R., Prasad, M., Kumar, G., Duranti, L., and Han, D. h., 2005, Seismic attenuation: observations and mechanisms, SEG Technical Program Expanded Abstracts, p. 1565-1568.

Bement, L. C., Carter, B. J., Varney, R. A., Cummings, L. S., and Sudbury, J. B., 2007, Paleo-environmental reconstruction and bio-stratigraphy, Oklahoma Panhandle, USA: Quaternary International, v. 169–170, no. 0, p. 39-50.

Berryman, J., 1995, Mixture theories for rock properties, *in* Ahrens, T. J., ed., American Geophysical Union Handbook of Physical Constants, : New York, AGU.

Brenders, A. J., and Pratt, R. G., 2007, Full waveform tomography for lithospheric imaging: results from a blind test in a realistic crustal model: Geophysical Journal International, v. 168, no. 1, p. 133-151.

Brossier, R., Operto, S., and Virieux, J., 2009, Seismic imaging of complex onshore structures by 2D elastic frequency-domain full-waveform inversion: Geophysics, v. 74, no. 6, p. WCC105-WCC118.

Chen, J., Jaiswal, P., and Zelt, C. A., 2013, A case history: Application of frequency-dependent traveltime tomography and full waveform inversion to a known near-surface target, SEG Technical Program Expanded Abstracts 2013, p. 1743-1748.

Claypoole, R. L., Baraniuk, R. G., and Nowak, R. D., Adaptive wavelet transforms via lifting, *in* Proceedings Acoustics, Speech and Signal Processing, 1998. Proceedings of the 1998 IEEE International Conference on1998, Volume 3, IEEE, p. 1513-1516.

Donoho, D. L., and Johnstone, J. M., 1994, Ideal spatial adaptation by wavelet shrinkage: Biometrika, v. 81, no. 3, p. 425-455.

Duncan, J. M., and Wright, S. G., 2005, Soil strength and slope stability.

Francese, R., Giudici, M., Schmitt, D. R., and Zaja, A., 2005, Mapping the geometry of an aquifer system with a high-resolution reflection seismic profile: Geophysical Prospecting, v. 53, no. 6, p. 817-828.

Gao, F., Levander, A., Pratt, R. G., Zelt, C. A., and Fradelizio, G.-L., 2007, Waveform tomography at a groundwater contamination site: Surface reflection data: Geophysics, v. 72, no. 5, p. G45-G55.

Gao, F., Levander, A. R., Pratt, R. G., Zelt, C. A., and Fradelizio, G. L., 2006, Waveform tomography at a groundwater contamination site: VSP-surface data set: Geophysics, v. 71, no. 1, p. H1-H11.

Gauthier, O., Virieux, J., and Tarantola, A., 1986, Two-dimensional nonlinear inversion of seismic waveforms: Numerical results: Geophysics, v. 51, no. 7, p. 1387-1403.

George, A., and Liu, J., 1981, Computer Solution of Large Sparse Positive Definite Systems, Englewood Cliffs, NJ, Prentice Hall.

Goodman, D., 1994, Ground-penetrating radar simulation in engineering and archaeology: Geophysics, v. 59, no. 2, p. 224-232.

Halliday, D. F., Curtis, A., Robertsson, J. O., and van Manen, D.-J., 2007, Interferometric surface-wave isolation and removal: Geophysics, v. 72, no. 5, p. A69-A73.

Hole, J. A., and Zelt, B. C., 1995, 3D finite-difference reflection traveltimes: Geophysical Journal International v. 121, p. 427-434.

Jaiswal, P., Zelt, C. A., Bally, A. W., and Dasgupta, R., 2008, 2-D traveltime and waveform inversion for improved seismic imaging: Naga Thrust and Fold Belt, India: Geophysical Journal International, v. 173, no. 2, p. 642-658.

Jaiswal, P., Zelt, C. A., Dasgupta, R., and Nath, K. K., 2009, Seismic imaging of the Naga thrust using multiscale waveform inversion: Geophysics, v. 74, no. 6, p. WCC129-WCC140.

Jo, C.-H., Shin, C., and Suh, J. H., 1996, An optimal 9-point, finite-difference, frequency-space, 2-D scalar wave extrapolator: Geophysics, v. 61, no. 2, p. 529-537.

Kamei, R., GerhardPratt, R., and TakeshiTsuji, 2012, Waveform tomography imaging of a megasplay fault system in the seismogenic Nankai subduction zone: Earth and Planetary Science Letters, v. 317–318, no. 0, p. 343-353.

Kumar, D., Sen, M. K., and Bangs, N. L., 2007, Gas hydrate concentration and characteristics within Hydrate Ridge inferred from multicomponent seismic reflection data: Journal of Geophysical Research: Solid Earth, v. 112, no. B12, p. B12306.

Londoño, E. G., López, L. C., and de Souza Kazmierczak, T., 2005, Using the Karhunen-Loève transform to suppress ground roll in seismic data: Earth Sciences Research Journal, v. 9, no. 2, p. 139.

Marfurt, K. J., 1984, Accuracy of finite-difference and finite-element modeling of the scalar and elastic wave equations: Geophysics, v. 49, no. 5, p. 533-549.

McBride, J. H., Stephenson, W. J., Williams, R. A., Odum, J. K., Worley, D. M., South, J. V., Brinkerhoff, A. R., Keach, R. W., and Okojie-Ayoro, A. O., 2010, Shallow subsurface structure of the Wasatch fault, Provo segment, Utah, from integrated compressional and shear-wave seismic reflection profiles with implications for fault structure and development: Geological Society of America Bulletin, v. 122, no. 11-12, p. 1800-1814.

Pellerin, L., Holliger, K., Slater, L., and Yaramanci, U., 2009, Special Issue on Hydrogeophysics - Methods and Processes Near Surface Geophysics, v. 7, no. 5-6, p. 303-305.

Pratt, R. G., 1999, Seismic waveform inversion in the frequency domain, Part 1: Theory and verification in a physical scale model: Geophysics, v. 64, no. 3, p. 888-901.

Press, W. H., Teukolsky, S. A., Vetterling , W. T., and Flannery, B. P., 1992, Numerical Recipes in C : the art of scientific computing, University Press.

Robertsson, J. O. A., Holliger, K., Green, A. G., Pugin, A., and De Iaco, R., 1996, Effects of near-surface waveguides on shallow high-resolution seismic refraction and reflection data: Geophys. Res. Lett., v. 23, no. 5, p. 495-498.

Romdhane, A., Grandjean, G., Brossier, R., Rejiba, F., Operto, S., and Virieux, J., 2011, Shallow-structure characterization by 2D elastic full-waveform inversion: Geophysics, v. 76, no. 3, p. R81-R93.

Sacchi, M., 2002, Statistical and transform methods in geophysical signal processing: Edmonton, Canada: Department of Physics, University of Alberta.

Scales, J. A., Docherty, P., and Gersztenkorn, A., 1990, Regularization of nonlinear inverse problems-imaging the near-surface weathering layer: Inverse Problems, v. 6, p. 115-131.

Sharma, P. V., 1997, Environmental and engineering geophysics, Cambridge University Press.

Shaw, P. R., and Orcutt, J. A., 1985, Waveform inversion of seismic refraction data and applications to young Pacific crust: Geophysical Journal International, v. 82, no. 3, p. 375-414.

Shieh, C.-F., and Herrmann, R. B., 1990, Ground roll: Rejection using polarization filters: Geophysics, v. 55, no. 9, p. 1216-1222.

Sirgue, L., and Pratt, R. G., 2004, Efficient waveform inversion and imaging: A strategy for selecting temporal frequencies: Geophysics, v. 69, no. 1, p. 231-248.

Smithyman, B., Pratt, R. G., Hayles, J., and Wittebolle, R., 2009, Detecting near-surface objects with seismic waveform tomography: Geophysics, v. 74, no. 6, p. WCC119-WCC127.

Strikwerda, J. C., 2004, Finite difference schemes and partial differential equations, Siam.

Sweldens, W., 1996, The lifting scheme: A custom-design construction of biorthogonal wavelets: Applied and computational harmonic analysis, v. 3, no. 2, p. 186-200.

Tarantola, A., 1984, Inversion of seismic reflection data in the acoustic approximation: Geophysics, v. 49, no. 8, p. 1259-1266.

Virieux, J., and Operto, S., 2009, An overview of full-waveform inversion in exploration geophysics: Geophysics, v. 74, no. 6, p. WCC1-WCC26.

White, J. E., 1975, Computed seismic speeds and attenuation in rocks with partial gas saturation: Geophysics, v. 40, no. 2, p. 224-232.

Yarham, C., and Herrmann, F. J., Bayesian ground-roll separation by curvelet-domain sparsity promotion, *in* Proceedings 2008 SEG Annual Meeting2008, Society of Exploration Geophysicists.

Zelt, C. A., Azaria, A., and Levander, A., 2006, 3D seismic refraction traveltime tomography at a groundwater contamination site: Geophysics, v. 71, no. 5, p. H67-H78.

Zelt, C. A., and Barton, P. J., 1998, Three-dimensional seismic refraction tomography: A comparison of two methods applied to data from the Faeroe Basin: Journal of Geophysical Research: Solid Earth (1978–2012), v. 103, no. B4, p. 7187-7210.

PAPER III

VELOCITY IMAGING WITH FULL WAVEFORM INVERSION IN THE ULTRA-SHALLOW SUBSURFACE, RESULTS FROM SH-WAVE DATA – PART 2

4.1 ABSTRACT

Shear (S) waves contain critical rock properties, yet they remain underutilized due to acquisition, processing and modeling related challenges. In this paper, 2D SH-wave data (S-wave polarization is perpendicular to the profile direction) are inverted using frequency domain Full Waveform Inversion (FWI) to generate fine-scale and interpretable velocity (V_S) and attenuation (Q_S^{-1}) maps in the ultra-shallow environment. The goal is to detect and differentiate between two targets – first, a set of water pipes with known diameters (0.6m and 0.75m) and burial depth (~1.5 m) and second, its former location that is now a backfilled void. The SH data are acquired using a static array of 24, 28 Hz horizontal component phones and a polarized source. Prior to FWI, ground roll is attenuated using two methods. First, through band pass filtering and muting. Second, through a novel wavelet transform based method known as the redundant lifting scheme (RLS). Results show that a) RLS better suppresses the ground roll coda which in turn aids FWI imaging; b) V_S and Q_S^{-1} could *differentiate* the anomalous zones but not *detect* them as precisely as their V_P and Q_P^{-1} counterparts (accompanying paper); and c) SH-wave modeling in addition to

conventional P-wave modeling can provide insights into the soil compaction in the ultra-shallow subsurface.

4.2 INTRODUCTION

Seismic refraction methods are being increasingly employed in detecting near-surface structures. Beyond their detection, being able to accurately reconstruct the physical properties of the host material plays an important role in engineering and environmental applications. In conventional seismic surveys P-wave data are recorded using vertical component phones. P-wave surveys have been widely used in near surface imaging both due to the ease of acquisition and wide availability of modeling algorithms. P-waves are affected by the bulk physical properties of the sediments, which includes both solid and liquid part. In contrast, shear (S-) waves do not propagate through fluids and could therefore in principle, characterize the solid matrix separately from effects of pore fluids.

The most popular method of building near surface S-wave velocity (V_S) models is through ground roll inversion (Xia et al., 1999; Xia et al., 2000). Although very successful in subsurface characterization (Beaty et al., 2002; Douma and Haney, 2011), in principle ground-roll inversion only provides Rayleigh wave velocities, which is then related to the V_S through simple transforms (Brown et al., 2000). Precise S-wave description from ground roll inversion may be difficult to obtain. First, Rayleigh waves are extremely dispersive, i.e., the phase velocity varies with frequency. To reconstruct V_S, a complete and balanced frequency spectrum is desirable, which may be difficult to obtain in ultra-shallow experiments where the wave attenuation is high

and non-uniform. Further, ground roll inversion hinges on interpreting the phase velocity versus frequency relationship, which can be subjective in the presence of poor data quality. On a related note, V_S estimation from ground roll inversion has mostly been done using P-wave data that are acquired with vertical component phones.

A second set of experiments for V_S modeling include direct recording of the horizontal ground motion using three component (3C) phones. Applications of 3C data in ultra-shallow investigations are not very common. Two representative case studies include Guevara et al. (2013) who used up-hole survey to compute near-surface V_S and De Meersman (2013) who modeled both V_S and S-wave attenuation (Q_S^{-1}) within the weathering layer in Alberta. The data in the two studies were acquired using explosive sources and the recorded shear waves were mainly mode-converted. In 3C surveys, data rotation is needed before S-waves amplitudes can be considered representative of subsurface reflection characteristics. If done improperly, data rotation could be a significant source of amplitudes errors.

A third way of obtaining S-wave data involves the experiment involves recording of horizontal motion when the source itself is polarized, i.e., it emits S-waves. The S-wave amplitudes in such cases, could be most reliable. Further, when the plane of polarization is orthogonal to the line of acquisition (the SH mode), the recoded data can be modeled assuming a P-like behavior. This idea is further explored in the present case study where SH-wave seismic data are inverted using a full waveform inversion (FWI) algorithm that was originally built to address P-wave propagation (Gauthier et al., 1986; Tarantola, 1984). In this algorithm the forward propagation

assumes a visco-acoustic earth model and the inverse problem is solved by iteratively updating a starting model to achieve a satisfactory misfit between the real and predicted wavefield (Pratt, 1999); the outcome is fine-scale geologically interpretable velocity and attenuation models.

The study area in this paper is located in Oklahoma State University's main campus in a sodded field overlying utility pipes. The target zones for SH imaging in the ultra-shallow depths (less than a few meters) are: a set of utility water pipes with known burial depth (1.5 m) and diameters (0.76 m), and a former location of one of the pipes, which is now a backfilled void. The location of the second target is not precisely known. The most challenging aspect of SH data processing is attenuating the Love Waves prior to FWI. Love waves, like Rayleigh Waves in P-wave data, are dispersive in nature. They are referred to as "ground roll" in this paper. Their successful separation from the body waves (SH in this case), is critical to the success of FWI. Like in the companion Paper from the results obtained for P-wave data, the raw SH data are processed conventionally (band pass filter and muting) as well as through application of redundant lifting scheme (RLS) producing two datasets for inversion. In an accompanying paper, hereafter referred to as Paper II in the dissertation, a P-wave velocity (V_P) and attenuation (Q_P^{-1}) model of the target zone has been prepared using frequency domain visco-acoustic FWI. In Paper II, the current and the former locations of the utility pipes appeared as V_P and Q_P^{-1} anomalies. Based on the magnitude or the polarity (percentage change over starting model) of the anomalies the two targets could not be differentiated. As a result, although they were "detected," they remained indistinguishable. In this paper, differentiation is tested with SH-wave following the same processing, modeling and inversion approach as in Paper II.

4.3 SURVEY AND DATA

The study area is located at the main campus of the Oklahoma State University (Figure 1a). The seismic data were acquired along a 23m long east-west (EW) profile (Figure 1b). The acquisition was planned keeping in view of their current and the former location of the pipe (Paper II). The profile is designed such that north-south oriented subsurface pipes are ~8m from the East end of the line leaving adequate imaging opportunity for the anticipated backfilled location which is towards the west of the pipes' current location. SH data were acquired using 28 Hz horizontal component geophone, firmly grounded in the soil to avoid oscillations. The source was a buried point-explosive. The shot holes were drilled at ~45^0 angle to the surface along a plane perpendicular to the seismic profile with the intent to excite the SH ground motion. The data were acquired in split-spread manner. Twenty-four receivers were placed 1m apart and sources were located in between the receivers. Altogether, a total of 552 traces were acquired from 23 shots. Recorded sampling interval and trace length were 0.125 ms and 500 ms respectively. Overall the data does not look as clean as their P-wave counterparts in Paper II, but the first arrivals wavelet could be identified to the farthest offsets (Figure 2). At the processing stage traces from -2.5 m to 2.5 m source-receiver offset are muted because of waveform clipping.

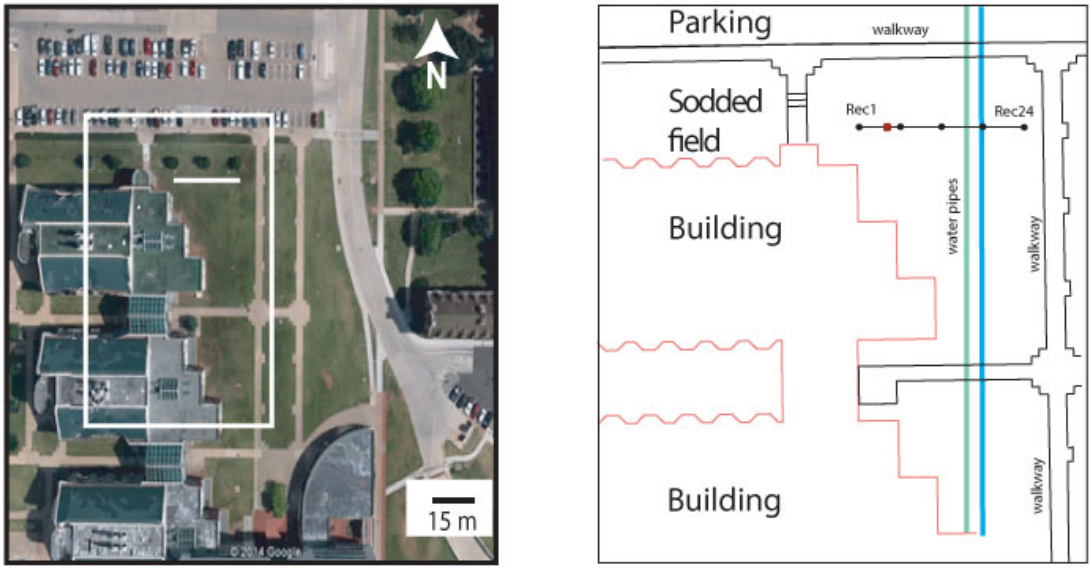

Figure 1: Base map. A) Google Earth image of Oklahoma State University's Main Campus. The study area is outlined with a white box. B) Sketch of the study area showing the location of the seismic line and the utility water pipes and the buildings. Data for the fifth source (red dot) is shown in Figure 2.

4.4 METHODOLOGY

Only a brief description of the processing and modeling methods is being provided here and the reader is guided to the original reference for more details.

4.4.1 DATA PROCESSING

Ground roll appears to be very strong in the field data (Figure 2a). Additionally, lower frequency and higher amplitude noise from instrument oscillations are also present. Other than the

conventional approach of band pass filtering and muting, a novel wavelet-transform based method known as redundant lifting scheme (RLS) (Claypoole et al., 1998) was also used for ground roll attenuation. The RLS is a modified version of an image processing method by Sweldens (1996) known as the Lifting Scheme (LS), which separates the signal and noise through wavelet transformations in time domain. The modification by Claypoole et al. (1998) from LS to RLS was mainly in preserving the entire signal length of the signal which eliminates the chances of aliasing (see Paper II of this dissertation for details).

4.4.2 INVERSION

Traveltime and waveform inversion, used in this paper are local decent methods implemented with the help of a smooth starting model which is iteratively updated. In the full waveform inversion, attenuation is implemented by assuming velocity as a complex quantity. For traveltime inversion, the regularized Zelt and Barton (1998) method is used. For waveform inversion, Pratt (1999) method is used. The traveltime inversion solves the eikonal equation using a scheme modified to handle large velocity variations (Hole and Zelt, 1995). The waveform method solves the visco-acoustic wave equation using the mixed-grid approach (Jo et al., 1996), which accounts for backscattering and wide-angle effects. The focus of the inversion part in both is to satisfy a convergence criteria but the formulation of the decent method and the stopping criteria are different (Paper II). Besides error reduction, geological interpretation plays an important role in deciding the success of both inversion methods. An important aspect of waveform inversion is its implementation using a multi-scale approach advocated by Bunks et al. (1995) to mitigate its non-linearity. This approach of solving the inverse problem proceeds from low to high

wavenumbers, using low temporal frequencies first and then refining the solution with higher frequency data.

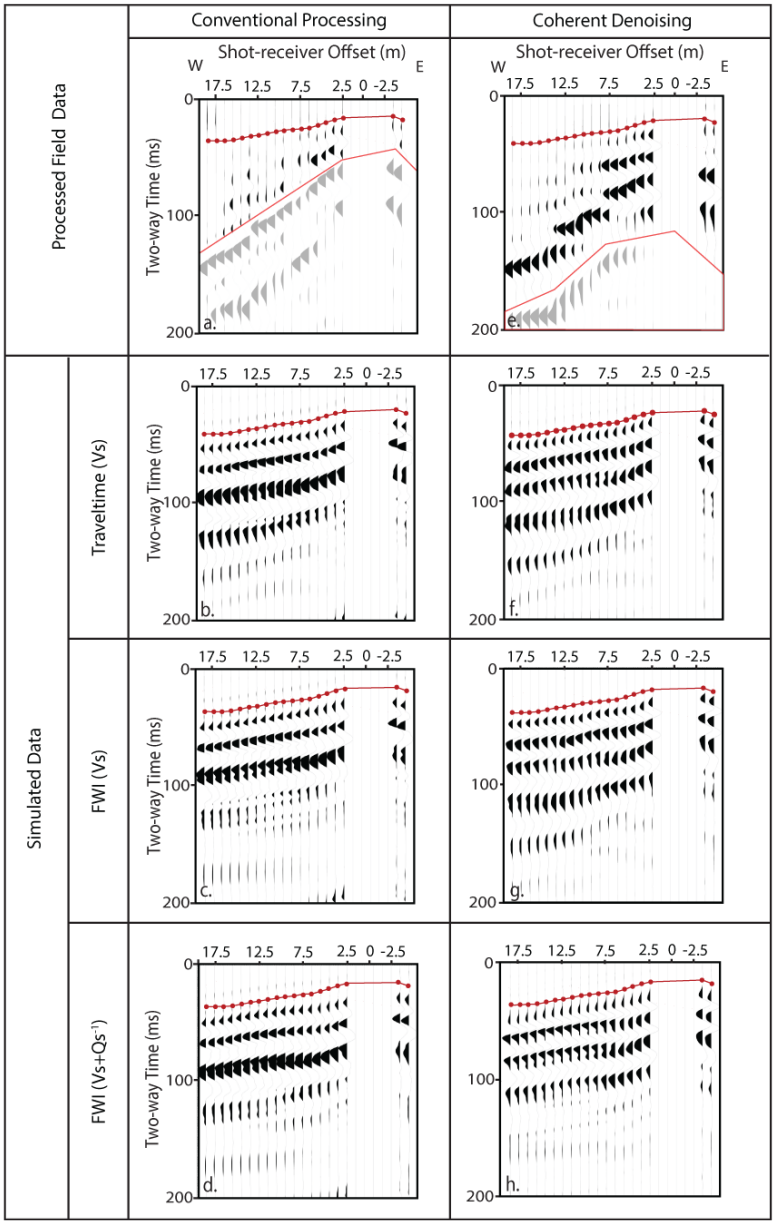

Figure 2: Representative data. a) Conventionally processed data. (b) – (d) simulated data from traveltime, FWI V_S, and FWI $V_S + Q_S^{-1}$ models. Models in (b) - (d) are obtained from inversion

of conventionally processed data. e) Coherent denoise data from RLS processing. (f) – (h) are same as (b) – (d) except that the models are obtained from inversion of coherent denoise data.

4.5 APPLICATION & RESULTS

The general workflow in this paper is same as Paper1 where the data are first preconditioned to remove phases that are beyond the physics of visco-acoutic modeling followed by first arrival traveltime inversion for generating a smooth V_S model which is then refined iteratively using FWI.

4.5.1 TRAVELTIME INVERSION

A total of 552 first arrival times were picked on 23 shot gathers. Based on dominant frequency and signal-to-noise ratio, an uncertainty of 2ms was assigned to all the picks. The staring model for the traveltime inversion was 1-D in nature. It comprised a linear gradient increasing from 100 m/s at the topography to 1200 m/s at the base of the model. The traveltime inversion converged in 12 iterations giving a smooth model (Figure 3a), which serves as the starting model for FWI.

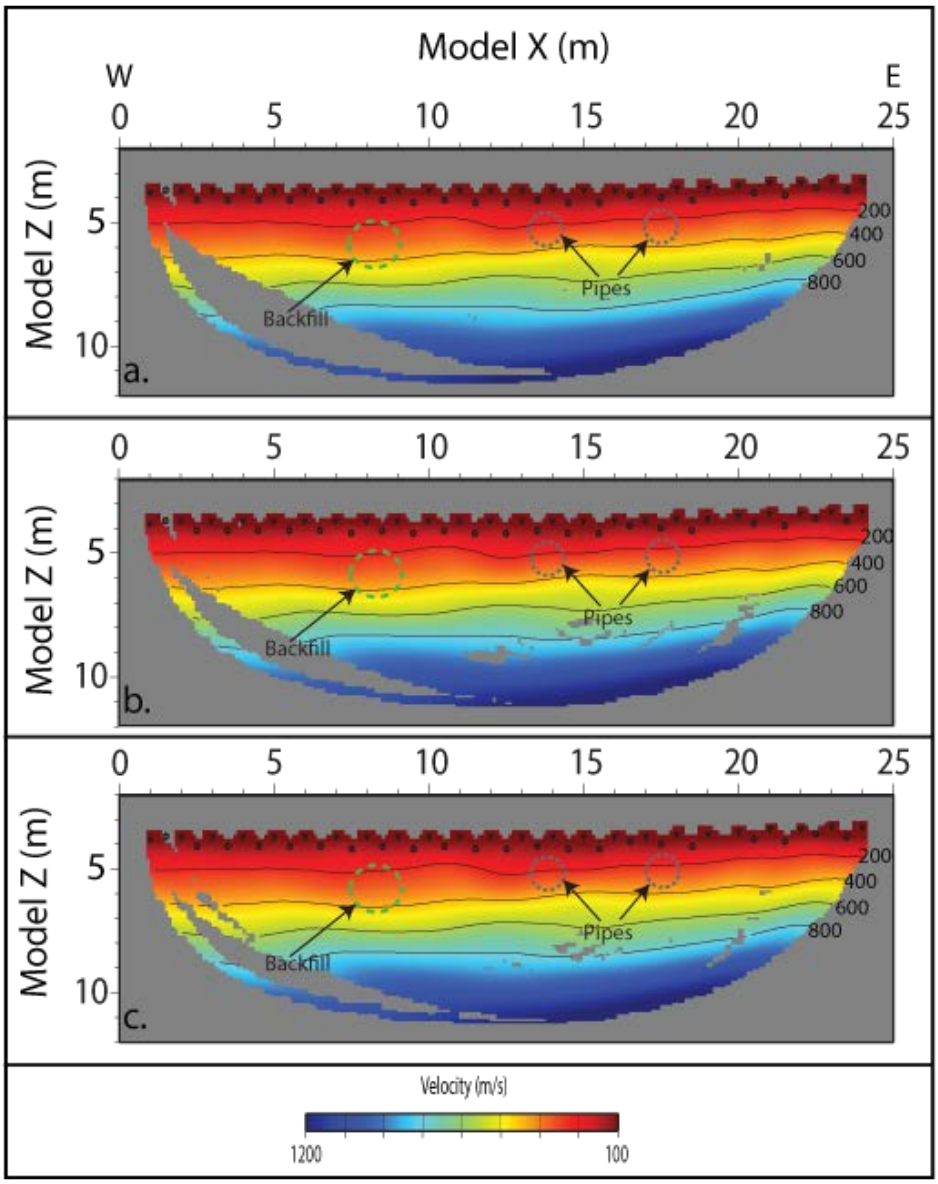

Figure 3: S-wave velocity (V_S) models from a) Travetime inversion. b) FWI of conventionally processed data. c) FWI of coherent denoise data. In (a) – (c) triangles and solid dots are the receiver and source locations. The current pipe locations are shown in black dashed circles. The former location, interpreted from Paper II and the perturbations (Figure 5), is outlined in green dashed circle.

4.5.2 DATA PREPARATION FOR FWI

The raw data were processed in two different ways in preparation for the FWI, both mainly aimed at attenuating the ground roll coda as effectively as possible without resulting in a loss of lower frequencies. The first method, which is a fairly conventional approach, includes 10-20-80-160 Hz band pass filtering, top mute above the first arrivals, a bottom mute to visually remove high-amplitude ground roll energy, data resampling at 1 ms and trace truncation at 200 ms. The dataset prepared using this method is hereafter referred to as conventionally processed data. The second method involves application of RLS followed by phase rotation. The dataset prepared using this method is hereafter referred to as coherent denoise data. In both datasets, a visual inspection is used to remove traces with low signal-to-noise ratio (S/N). In the end both datasets comprised 414 traces. Amplitude scaling was applied to both datasets in order to match their amplitude-versus-offset (AVO) trend with simulated data generated by starting (traveltime) model and the initial Ricker source.

4.5.3 SOURCE AND MODEL UPDATE

With both datasets, FWI begins with the estimation of source signature (Figure 4a and d) using the starting model (Figure 3a). Following this, the lowest frequency in the SH data, ~25 Hz, was inverted. Almost no updates in the starting model were obtained from inversion of frequencies up to 35Hz. The first group of frequencies that yielded reasonable updates was 35, 40 and 45 Hz. These frequencies were simultaneously inverted using the source obtained from the traveltime model. The updates from inversion of this frequency group (Figure 5a and d), were smooth and appropriately located around the targets. Higher frequencies were incorporated in a bootstrap

manner. The V_S model from one set of inversion frequencies was used as the starting model for next set. The source signature was updated in between two sets of inversion frequencies using the current model, yielding a broader band source at every step (Figure 4). In each inversion run, model updates were sought until the reduction in objective function was below 1%. Past the lowest frequency group significant V_S updates were obtained only from two more frequency groups - 55, 60, 65 Hz and 60, 65, 70 Hz (Figure 5b and e) and 75, 80, 85 Hz (Figure 5c and f). Frequencies above 85 Hz made the model noisier result in model updates which could not be related to any known (or expected) model anomalies. A judgment call was made to halt the inversion at 85 Hz.

The V_S inversion was followed by Q_S^{-1} inversion. The final FWI V_S model from conventionally processed data (Figure 5c) and coherent denoise data (Figure 5f) were used as the initial velocity models. The initial attenuation model was set to zero. Unlike the general practice with the P-waves, e.g., in Paper II, frequency groups used for V_S inversion did not provide reasonable attenuation updates; not only were the resulting Q_S^{-1} model noisy, the inversion diverged even at the lowest frequency group (35 – 45 Hz). The most meaningful results were obtained by inverting 25-30-35 Hz (Figure 6a). At this stage it is not clear why the lowest useable frequencies for V_S and Q_S^{-1} inversion are different. In principle, frequencies for velocity and attenuation inversion need not be the same, but it is a general practice to do so. The other frequency groups that resulted in reasonable attenuation updates were 40-45-50 Hz (Figure 6b) and 55-60-65 Hz (Figure 6c). On similar lines, the minimum usable frequency group for data processed using the RLS was 40-45-50 Hz (Figure 6d), which is much higher than the first set of processes data. The other frequency groups that resulted in reasonable updates were 55-60-65

Hz (Figure 6e), and 80-85-90 Hz (Figure 6f). For both datasets, inversion was halted based on the mode stability, convergence of objective function and geological reasonability of the model updates.

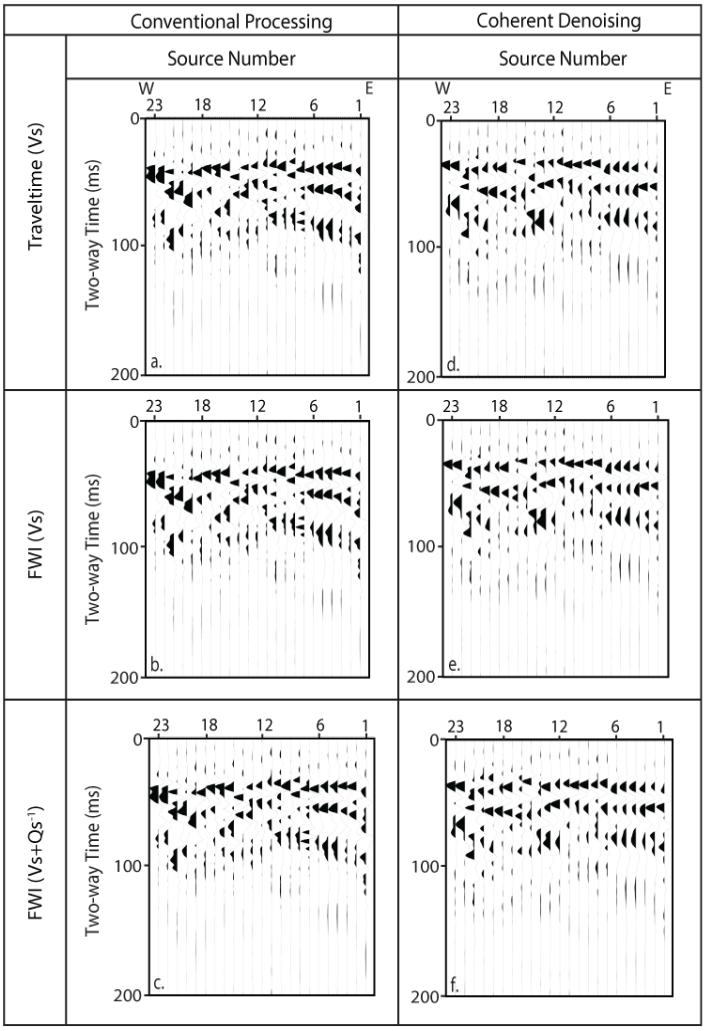

Figure 4: Inverted Sources. a) Traveltime V_S model, b) FWI V_S model and c) combined FWI V_S and S-wave attenuation (Q_S^{-1}) models. Models in (a) – (c) are obtained by inverting conventionally processed data and (d) – (f) are obtained by inverting coherent denoise data. Sources successively become more consistent as velocity and attenuation models are created.

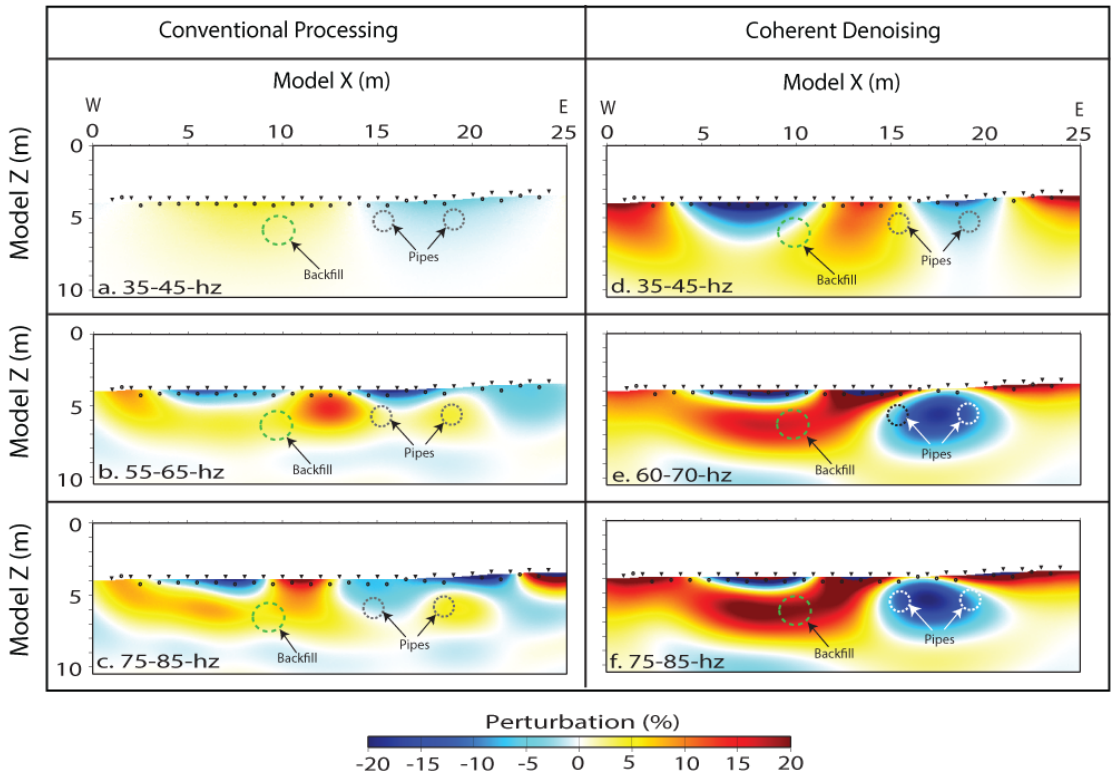

Figure 5: FWI V_S perturbations. (a) 35-40-45 Hz, (b) 55-60-65 Hz and (c) 75-80-85 Hz inversion models from conventionally processed data. (d) 35-40-45 Hz, (e) 60-65-70 Hz and (f) 75-80-85 Hz inversion models from coherent denoise data. In (a) – (f) current pipe locations are represented by two eastern dashed circles. Former pipe location, based on Paper II, is outlined in green dashed circle.

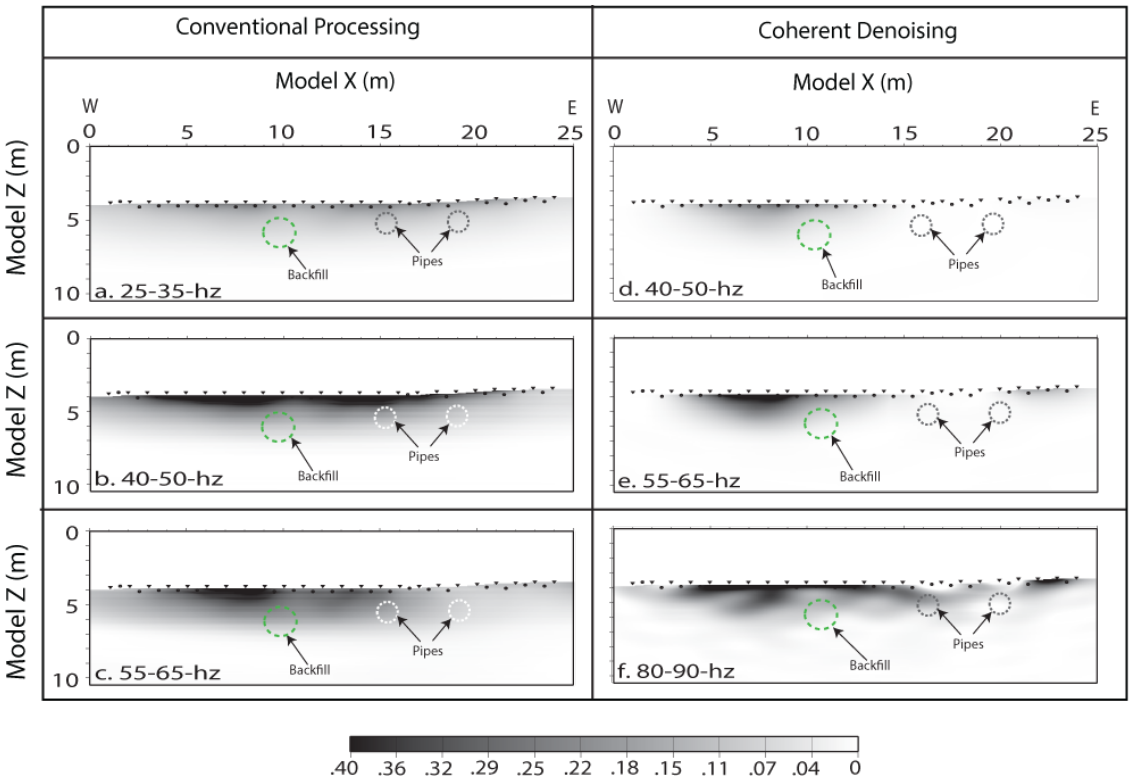

Figure 6: FWI Q_S^{-1} models. (a) 25-30-35 Hz (b) 40-45-50 Hz, and (c) 55-60-65 Hz inversion models from conventionally processed data. (d) 40-45-50 Hz, (e) 55-60-65 Hz and (f) 80-85-90 Hz inversion models from coherent denoise data. In (a) – (f) current pipe locations are represented by two eastern dashed circles. Former pipe location, based on Paper II, is outlined in green dashed circle.

4.5.4 MODEL ASSESSMENT

The final FWI V_S models from both datasets showed perturbation of the order of ±20% with respect to the starting model. The fidelity of these perturbations was tested through single

anomaly tests, where the starting model was perturbed in line with the final model. Introducing -20% perturbation at the location of water pipes and +20% at the location of the suspected

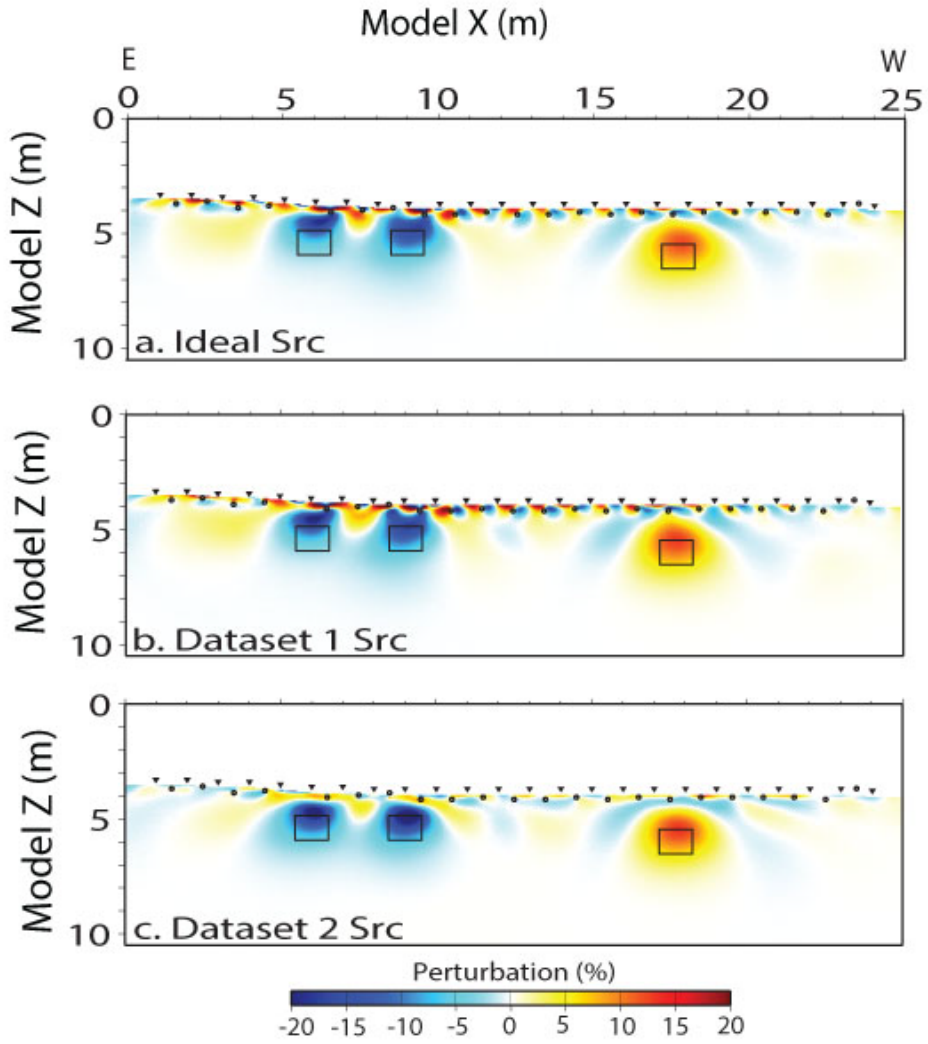

Figure 7: Resolution test. (a) Ideal source (b) Final extracted source from conventionally processed data (c) Extracted source from coherent denoise data. In (a) – (c) the induced anomaly location are outlined in solid black boxes. The perturbation magnitude was 20%.

backfilled void, three synthetic datasets were simulated using a) an ideal source; b) the final inverted source from conventionally processed data (Figure 4c); and c) the final inverted source from coherent denoise data (Figure 4f). These data were inverted in the same manner as the real data. Figure 7 indicates that the anomalies could be recovered in all three cases suggesting that a) the starting model had adequate resolution to allow the FWI to start at 35 Hz, and b) the anomalies in the final FWI perturbation model are realistic which can be interpreted for a geological feature.

The final models were further assessed by comparing the first arrival and root mean square (RMS) amplitudes of both datasets with their counterparts simulated from the traveltime and FWI models with respective sources (Figure 8). Figures 8a, b and c show the first arrival errors respectively corresponding to traveltime, FWI V_S and FWI V_S+Q_S^{-1} models for conventionally processed data. Figures 8d – f are same as a – c, computed for coherent denoise data. Figures 8g, h and i are RMS errors respectively corresponding to traveltime, FWI V_S and FWI V_S+Q_S^{-1} models for conventionally processed data. Figures 8j – l are same as g – i, computed for coherent denoise data.

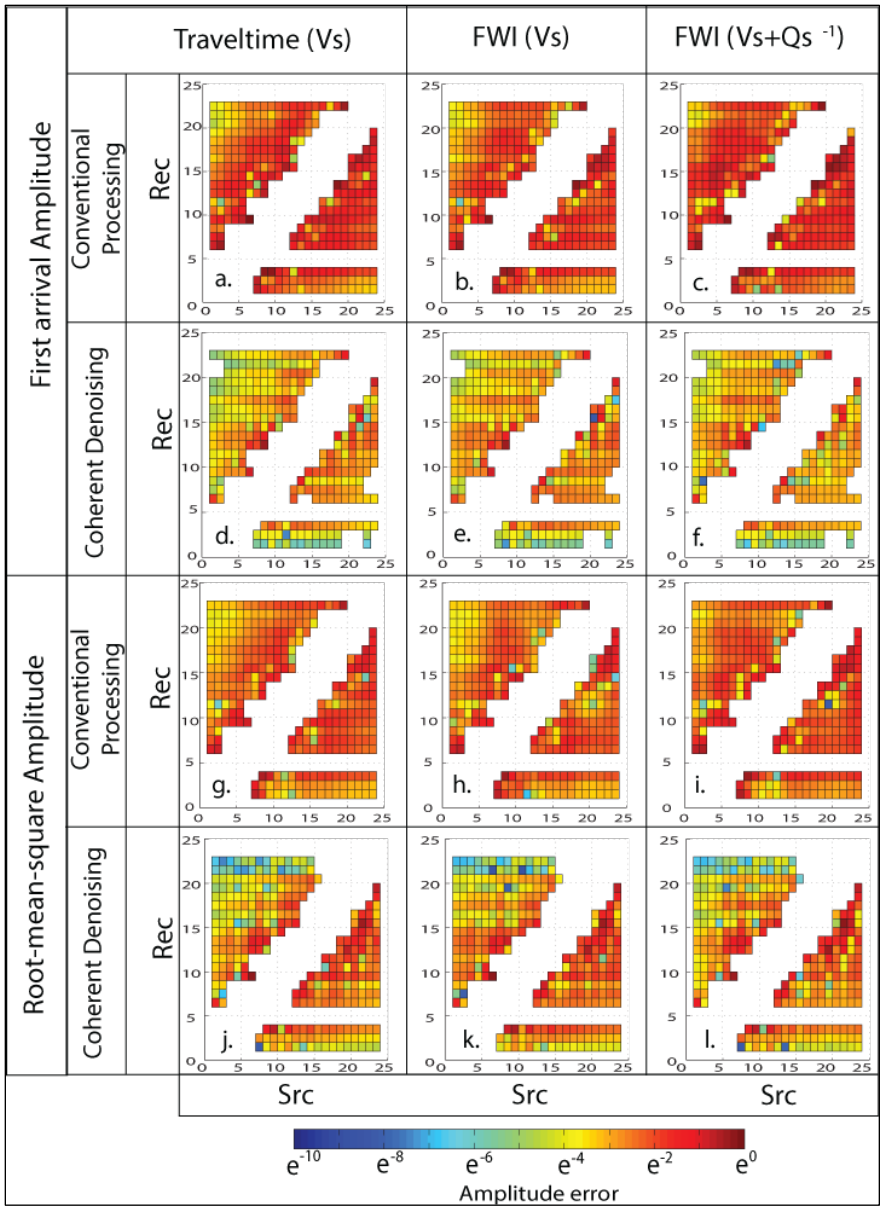

Figure 8: Amplitude comparison. Difference in first arrival amplitude between conventionally processed and simulated data from a) traveltime V_P and the corresponding inverted source, b) FWI V_P and the corresponding inverted source and c) FWI V_S + Q_S^{-1} and the corresponding inverted source. (d) – (f) are same as (a) – (c) except that results are for coherent denoised data. (g) – (l) same as (a) – (f) except that the results are for whole trace root-mean-square amplitude.

In figure 8, warmer colors represent higher error. As evident, data simulated with FWI $V_S + Q_S^{-1}$ model do not appears to be getting closer to respective inputs in all cases. For example, the first arrival or RMS errors in conventionally processed data show little to no improvement from FWI process. This is resonated in Figure 5 as well where the evolving perturbations from inverting conventionally processed data have no coincidence with expected targets. Even for coherent denoised data, improvements through FWI in both first arrival and RMS errors are rather marginal although the overall error for coherent denoised data is much less than that for conventionally processed data. In contrast to Paper II, where inclusion of Q_P^{-1} in forward modeling deteriorates the data fit (Paper II), here inclusion of Q_S^{-1} slightly improves the fit. It is notable that this is despite the fact that unlike Q_S^{-1}, the Q_P^{-1} model was actually closer to its velocity counterpart. Like in Paper II, although the improvement in amplitude far from FWI is rather marginal, the V_S perturbations from FWI of coherent denoised data (Figures 8f) could be considered reliable.

For additional visual comparison, simulated data were also presented in the time-offset domain (Figure 2a-d for conventionally processed data and 2e-h for coherent denoised data). The representative data show a very marginal improvement through the FWI process, particularly compared to their P-wave counterparts in Paper II. The attenuation character of the real data is very strong and could not be well replicated by FWI. It is possible that complex velocities may not be the correct way of implementing SH attenuation.

4.5.5 RESULTS

The spatial location of the targets can be better identified in the V_S perturbation model from coherent denoised data (Figures 5f). Perturbations at the known location of the utility pipes is more focused in Figure 5f than at the expected backfilled location (Paper II), where the velocity is updated at the corrected depth (1.5m; Paper II) but is laterally smeared. V_S perturbation related to water pipes is negative (V_S decreases with respect to the starting model) and backfilled void is positive. The increase in V_S in the backfield area is probably due to compaction from filling the void.

The attenuation models from both datasets do not follow the V_S perturbations. In fact none of the attenuation models show any distinct anomalies. The attenuation models merely seem to be implying that the near-surface is highly attenuative, which is as intuitively expected. A lack of attenuation structures near the targets does not necessarily mean that the attenuation models are inaccurate. S-waves attenuation is rather poorly understood and it is not clear if they are supposed to be interpreted as their P-wave counterparts. It is notable that FWI V_P in Paper II could locate the anomalous features but could not differentiate between them. On the other hand, the V_S models appear to be having opposite polarity perturbations at the current and former pipe locations but the perturbations are not as focused as their P-wave counterparts.

Combining the V_P models from Paper II (Figure 7f; Paper II) with V_S model in this paper (Figure 5f), a Poisson's ratio (PR) model can be computed (Figure 9). In the zone of the current pipe locations the PR values are higher than the background. The inverse is seen at the zone

interpreted as former pipe location. Higher PR represents a higher V_P/V_S ratio and *vice-versa*. Lower PR in the interpreted backfilled zone indicates similar V_P and V_S values, which could be due to compaction in the process of backfilling that disproportionately increased the V_S. The background material, which is mainly loose soil, has lower V_P than water. In the zone with utility water pipes, presence of water may have enhanced V_P while leaving the V_S unaffected, thus resulting in a higher PR.

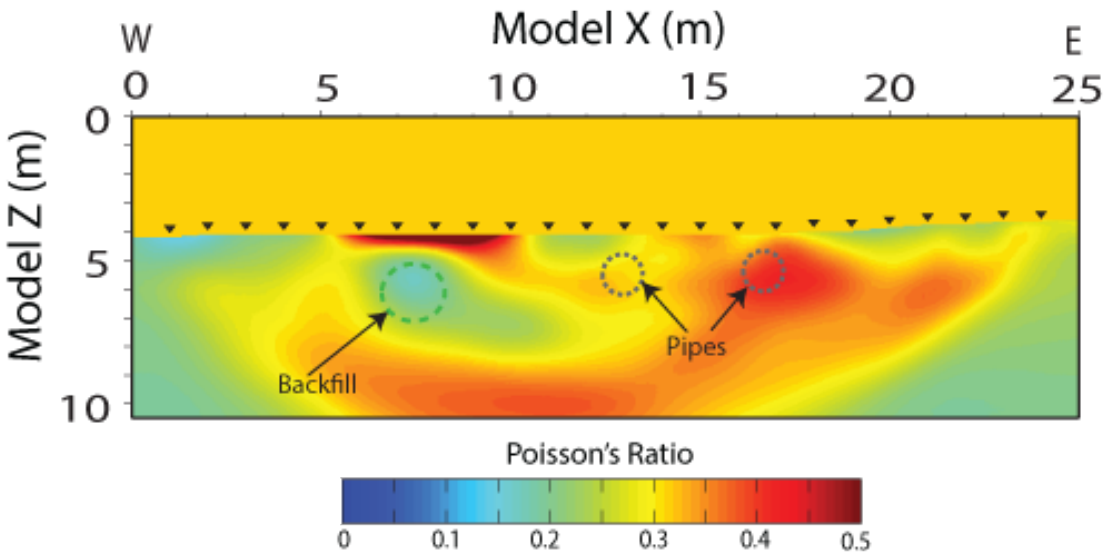

Figure 9: Poisson's ratio model from the FWI V_P (Figure 5; Paper II) and V_S (Figure 3) models. Current pipe locations are shown in solid black boxes and the former pipe location is interpreted in dashed ellipse. Current and former pipes locations respectively have high and low PR.

4.6 DISCUSSION

First break amplitudes in coherent denoise data showed more improvement from traveltime to full-waveform V_P inversion as compared to the next step, which was additional full-waveform Q_P^{-1} inversion. On the other hand, first break amplitudes in conventionally processed data showed little to no improvements from traveltime to full-waveform V_P (or V_P+Q_P^{-1}) inversion. This was probably due to a better data preconditioning from RLS application. In conventionally processed data, the RMS amplitude errors deteriorate marginally from traveltime to FWI, suggesting that the inversion could have created model artifacts. It appears that ground roll removal helped improve the overall data quality. Ground roll removal through RLS has also attenuated the low-frequency instrument oscillations that were not easily quantifiable.

The V_S perturbations (% change with respect to the starting model) were more reliable than the whole V_S values themselves (Figure 5 versus Figure 3). This was due to two reasons. First, imaging targets in this paper were not geological features with measurable physical properties, but rather perturbations in an otherwise stationary background medium. In a sense, the magnitude of velocity perturbations in FWI was meaningless. It was the location and the polarity of the perturbation that can be interpreted in terms of the cause of perturbation. Second, bulk density was the key parameter used in FWI. In absence of laboratory measurements, it was common to assign density as a function of velocity. In Paper II Gardner's relation (Gardner et al., 1974) was used, which relates the bulk density with V_P. Since density as a function of V_S in the near surface was unavailable, while inverting the SH data bulk density was fixed to 1.0 g/cc. Not

considering density variation could also be one of the reasons why improvements in amplitude fit from FWI was rather marginal as compared to Paper II.

S-wave's insensitivity to fluid can be implemented and differentiate medium physical properties. Researchers have routinely inverted P-wave data in the near surface (Fesseha Woldearegay et al., 2012; Smithyman et al., 2009). P-wave modeling is valuable in basin-scale investigations when the background sediment matrix is fairly well-constrained and velocity anomalies can be directly related to porosity or fluid-content changes. Sediment properties rapidly change in the first few meters. Particularly, in the vadose zone, which can vary from less than a meter to few meters only, partial saturation with air, saline or freshwater (and occasionally contaminants), can drastically affect V_P. In such cases, incorporation of SH-wave modeling along with the conventional P-waves could be very useful in detecting subtle lithologic changes.

Estimation of V_S from FWI of SH- data remains a largely unexplored method in near surface geophysics. This paper was one of the pioneering efforts in FWI of S_H data and shows that with careful acquisition, processing and modeling; S_H data can be yield valuable information about the subsurface soil character. At a first look, the S_H-wave data appears to be much noisier than their P-wave counterparts in Paper II. The intent of processing data in two different ways prior to FWI was to check how much processing effects the quality of the inversion. Conventionally processed data failed to yield any meaningful result from inversion. Data processed using RLS showed opposite polarities at the target location. Like in Paper II, exploring other ways of

ground roll suppression is out of this paper's scope but it will be fair to say that effective processing can greatly influence FWI in the ultra-shallow environments.

The most significant outcome of SH-wave inversion was velocity updates with opposite polarity associated with water pipes and backfilling. The attenuation images do not appear to be synchronous with the velocity character like their P-waves counterparts in Paper II. This should not be necessarily interpreted as a shortcoming or limitation of the process of attenuation inversion. At the pipe location, the background medium could have been more attenuated than the targets themselves. At the backfilled location an increase in compaction may have discouraged attenuation but at this stage the reasons and the mechanisms of SH attenuation are not fully understood.

Results in this paper were complimentary to results in Paper II. In Paper II the cold water pipes and the backfilled void appeared as zones of V_P increase. Based on the magnitude or polarity of the enhancements, the two targets could be located but not differentiated. In this paper, in terms of V_S, the polarity of the velocity updates were opposite in the general target location. These partial definitions of the anomalies were not as clear as in Paper II, but the fact that their physical properties may be different was very clear. When both the images were combined together as a PR model, the target images were focused as well has opposite characteristics with respect to the background. It appears that acquisition of SH waves in addition to P-waves can be a very useful tool in characterizing the ultra-shallow subsurface.

4.7 CONCLUSIONS

This paper is a pioneering case study of characterizing ultra-shallow subsurface using traveltime and full-waveform inversion of SH-wave data. Data preconditioning, which is attenuation of Love Waves in this case, and construction of a starting model with wavenumber content equivalent to the missing low frequencies in the real data are crucial to FWI's success. When compared in Paper II, it appears that the SH-waves can better differentiate physical properties of the soil with utility pipes from their former, backfilled location. Thus a combination of both P- and SH- data analysis can be greatly beneficial in ultra-shallow investigations.

4.8 ACKNOWLEDGMENTS

The seismic data in this study were acquired with the help of Salman Abbasi, Pouyan Ebrahimi and Brooke Briand. The physical plant at Oklahoma State University provided the blueprint and scoped the problem. SEG student chapter partially funded the survey.

4.9 REFERENCES

Beaty, K., Schmitt, D., and Sacchi, M., 2002, Simulated annealing inversion of multimode Rayleigh wave dispersion curves for geological structure: Geophysical Journal International, v. 151, no. 2, p. 622-631.

Brown, L., Diehl, J. G., and Nigbor, R. L., A simplified procedure to measure average shear-wave velocity to a depth of 30 meters (VS30), *in* Proceedings of 12th world conference on earthquake engineering 2000.

Bunks, C., Saleck, F. M., Zaleski, S., and Chavent, G., 1995, Multiscale seismic waveform inversion: Geophysics, v. 60, no. 5, p. 1457-1473.

Claypoole, R. L., Baraniuk, R. G., and Nowak, R. D., Adaptive wavelet transforms via lifting, *in* Proceedings Acoustics, Speech and Signal Processing, 1998. Proceedings of the 1998 IEEE International Conference on1998, Volume 3, IEEE, p. 1513-1516.

De Meersman, K., 2013, S-waves and the near surface: A time-lapse study of S-wave velocity and attenuation in the weathering layer of an Alberta heavy oil field: The Leading Edge, v. 32, no. 1, p. 40-47.

Douma, H., and Haney, M., Surface-wave inversion for near-surface shear-wave velocity estimation at Coronation field, *in* Proceedings 81st SEG Annual Meeting2011, p. 1411-1415.

Fesseha Woldearegay, A., Jaiswal, P., Simms, A. R., Alexander, H., Bement, L. C., and Carter, B. J., 2012, Ultrashallow depth imaging of a channel stratigraphy with first-arrival traveltime inversion and prestack depth migration: A case history from Bull Creek, Oklahoma: Geophysics, v. 77, no. 2, p. B87-B96.

Gardner, G. H. F., Gardner, L. W., and Gregory, A. R., 1974, Formation Velocity And Density - Diagnostic Basics For Stratigraphic Traps: Geophysics, v. 39, no. 6, p. 770-780.

Gauthier, O., Virieux, J., and Tarantola, A., 1986, Two-dimensional nonlinear inversion of seismic waveforms: Numerical results: Geophysics, v. 51, no. 7, p. 1387-1403.

Guevara, S. E., Margrave, G. F., and Agudelo, W. M., 2013, Near-surface S-wave velocity from an uphole survey using explosive sources.

Hole, J., and Zelt, B., 1995, 3-D finite-difference reflection traveltimes: Geophysical Journal International, v. 121, no. 2, p. 427-434.

Jo, C.-H., Shin, C., and Suh, J. H., 1996, An optimal 9-point, finite-difference, frequency-space, 2-D scalar wave extrapolator: Geophysics, v. 61, no. 2, p. 529-537.

Pratt, R. G., 1999, Seismic waveform inversion in the frequency domain, Part 1: Theory and verification in a physical scale model: Geophysics, v. 64, no. 3, p. 888-901.

Smithyman, B., Pratt, R., Hayles, J., and Wittebolle, R., 2009, Detecting near-surface objects with seismic waveform tomography: Geophysics, v. 74, no. 6, p. WCC119-WCC127.

Sweldens, W., 1996, The lifting scheme: A custom-design construction of biorthogonal wavelets: Applied and computational harmonic analysis, v. 3, no. 2, p. 186-200.

Tarantola, A., 1984, Inversion of seismic reflection data in the acoustic approximation: Geophysics, v. 49, no. 8, p. 1259-1266.

Xia, J., Miller, R. D., and Park, C. B., 1999, Estimation of near-surface shear-wave velocity by inversion of Rayleigh waves: Geophysics, v. 64, no. 3, p. 691-700.

Xia, J., Miller, R. D., Park, C. B., Hunter, J. A., and Harris, J. B., 2000, Comparing shear-wave velocity profiles from MASW with borehole measurements in unconsolidated sediments, Fraser River Delta, BC, Canada: Journal of Environmental & Engineering Geophysics, v. 5, no. 3, p. 1-13.

Zelt, C. A., and Barton, P. J., 1998, Three-dimensional seismic refraction tomography: A comparison of two methods applied to data from the Faeroe Basin: Journal of Geophysical Research: Solid Earth (1978–2012), v. 103, no. B4, p. 7187-7210.

APPENDICES

APPENDIX A: ESTIMATION OF THE FRESNEL ZONE WIDTH

The cross sectional radius of the first Fresnel zone can be expressed as a function of the source – receiver offset, D, as (Tomasi, 1987):

$$F_n = \frac{1}{2}\sqrt{\frac{ncD}{f}}, \qquad \text{(A1)}$$

where, F_n is the *n*th Fresnel Zone radius, *c* is the velocity and *f* is the dominant frequency of the data.

Consider the vertical component dataset that has a dominant frequency of 100 Hz and a background velocity of 200 m/s. For the smallest source-receiver offset, *D=1 m*, Eq. A1 yields $F_1 = 0.70\,m$. Likewise, for an intermediate source-receiver offset, *D=5 m*, Eq. A1 yields $F_1 = 1.58\,m$; for larger source-receiver offset, *D=15 m*, Eq. A1 yields $F_1 = 2.7\,m$. Ray coverage at the target depths is mainly from 1 to 5 m offsets and therefore the expected width of the first Fresnel Zone is between 0.7 and 1.5 m.

Similarly, consider the tangential component dataset that has a dominant frequency of 60 Hz and a background velocity of 100 m/s. For a source-receiver offset of 1 m, Eq. A1 yields $F_1 = 0.65\,m$. Likewise, for source-receiver offsets of 5 and 15 m, Eq. A1 yields $F_1 = 1.44\,m$ and $F_1 = 2.5\,m$, respectively. Ray coverage at the target depths is mainly from 1 to 5 m offsets and therefore the expected width of the first Fresnel Zone is between 0.65 and 1.44 m, which are comparable to the vertical dataset.

APPENDIX-B

$$E(m)^{TT} = \Delta d^T C_d^{-1} \Delta d + \lambda[m^T C_h^{-1} m + s_z m^T C_v^{-1} m] \quad (15)$$

$$E(m) = \delta d^T {C_d}^{-1} \delta d + \lambda[m^T {C_h}^{-1} m + s_z m^T {C_v}^{-1} m]$$

Let,

E= part1 + part2; where, part1 = $\delta d {C_d}^{-1} \delta d$, and part2 = $\lambda[m^T {C_h}^{-1} m + s_z m^T {C_v}^{-1} m]$. Hence if the derivative of both part1 and part2 are 0, the derivative of E will also be 0.

By taking the derivative on left side:

$$\frac{\partial E(m)}{\partial m} = 0$$

Now taking the derivative of part2 of RHS of the equation:

$$\frac{\partial}{\partial m}(\lambda\left[m^T {C_h}^{-1} m + s_z m^T {C_v}^{-1} m\right]) = 0$$

$$\Rightarrow \lambda[\frac{\partial}{\partial m}\left(m^T {C_h}^{-1} m\right) + \frac{\partial}{\partial m}(s_z m^T {C_v}^{-1} m)] = 0$$

$$\Rightarrow \lambda[m\left({C_h}^{-1} + ({C_h}^{-1})^T\right) + s_z m\left({C_v}^{-1} + ({C_v}^{-1})^T\right)] = 0; \text{ [Using} \frac{\partial x^T B x}{\partial x} = (B + B^T)x]$$

$$\Rightarrow \lambda[m\left({C_h}^{-1} + {C_h}^{-1}\right) + s_z m\left({C_v}^{-1} + {C_v}^{-1}\right)] = 0; \text{ [For Symmetric matrices } M^T = M]$$

$$\Rightarrow \lambda[2m{C_h}^{-1} + 2s_z m{C_v}^{-1}] = 0$$

$$\Rightarrow 2\lambda m{C_h}^{-1} = -2s_z \lambda m{C_v}^{-1} \quad \text{(B1)}$$

Given,

$$m = m_0 + \delta m \quad \text{(B2)}$$

Replacing m in equation A1:

$$\Rightarrow 2\lambda(m_0 + \delta m){C_h}^{-1} = -2\lambda s_z(m_0 + \delta m){C_v}^{-1};$$

$$\Rightarrow 2\lambda m_0 {C_h}^{-1} + 2\lambda \delta m {C_h}^{-1} = -2\lambda s_z m_0 {C_v}^{-1} - 2\lambda s_z \delta m {C_v}^{-1}$$

$$\Rightarrow \lambda m_0 {C_h}^{-1} + \lambda \delta m {C_h}^{-1} = -\lambda s_z m_0 {C_v}^{-1} - \lambda s_z \delta m {C_v}^{-1} \quad \text{(B3)}$$

Again taking the derivative of first part:

$$\frac{\partial}{\partial m}(\delta d^T {C_d}^{-1} \delta d) = 0$$

$\Rightarrow \delta d^T({C_d}^{-1} + ({C_d}^{-1})^T)\frac{\partial(\delta d)}{\partial m}\partial m = 0$; [Using chain rule]

$$\Rightarrow \delta d^T \frac{\partial(\delta d)}{\partial m}\partial m = 0$$

$\Rightarrow [L]\partial m = (\delta d^T)^{-1}$; [Given L is the partial derivative matrix]

$$\Rightarrow \left[{C_d}^{-1/2} L\right]\partial m = \left[{C_d}^{-1/2}\delta d\right] \quad \text{(B4)}$$

Combining equation (B3) and (B4)

$$\begin{bmatrix} {C_d}^{-\frac{1}{2}} L \\ \lambda C_h \\ s_z \lambda C_v \end{bmatrix} \delta \boldsymbol{m} = \begin{bmatrix} {C_d}^{-\frac{1}{2}} L \\ -\lambda C_{hm_0} \\ -s_z \lambda C_v m_0 \end{bmatrix}$$

VITA

Md. Iftekhar Alam

Candidate for the Degree of
DOCTOR OF PHILOSOPHY

Thesis: NEAR-SURFACE CHARACTERIZATION USING TRAVELTIME AND

WAVEFORM INVERSION

Major Field: GEOLOGY

Biographical:

Education:

Completed the requirements for the Doctor of Philosophy in Geology at Oklahoma State University, Stillwater, Oklahoma in December, 2015.

Completed the requirements for the Master of Science in Geology from the Department of Geosciences, Auburn University, Auburn, AL, 2011.

Completed the requirements for the Master of Science in Petroleum Geology and Geophysics from Department of Geology at University of Dhaka Dhaka, Bangaldesh, 2009.

Completed the requirements for the Bachelors of Science in Geology from Department of Geology at University of Dhaka Dhaka, Bangaldesh, 2006.

Experiences:

Teaching and Research Assistant, Boone Pickens School of Geology August 2011-December 2016.

Teaching Assistant, Department of Geosciences, Auburn University, August 2009-July 2011.

Professional Memberships:
Society of Exploration Geophysicists (SEG)
American Geophysical Union (AGU)
American Association of Petroleum Geologists (AAPG)
Geological Society of America (GSA)
Geophysical Society of Oklahoma City (GSOC)